

1 **Contribution of magmatism, partial melting buffering and localized crustal thinning on the**
2 **late-variscan thermal structure of the Agly massif (French Pyrenees)**

3
4 Siron Guillaume^{1,2}, Goncalves Philippe¹, Marquer Didier¹, Pierre Trap¹, Paquette Jean-Louis³,
5 Vanardois Jonas¹

6
7 ¹ *Laboratoire Chrono-environnement, Université de Bourgogne Franche-Comté, CNRS, Besançon,*
8 *France.*

9 ² *WiscSIMS Laboratory, University of Wisconsin-Madison, Madison, United States of America.*

10 ³ *Laboratoire Magmas et Volcans, Université Clermont-Auvergne, CNRS, IRD, OPGC, Clermont-*
11 *Ferrand, France.*

12

13 Corresponding author: siron@wisc.edu

14

15 **Abstract**

16 Low pressure-high temperature (LP-HT) metamorphism, with geothermal gradients in the order of
17 50 to 100°C/km, is a common feature of the late evolution of collisional orogens. These abnormal
18 thermal conditions may be the results of complex interactions between magmatism, metamorphism
19 and deformation. The Agly massif, in the French Pyrenees, preserves the metamorphic footprints of
20 the late Variscan thermal structure of an almost continuous section from the upper and middle
21 continental crust. The upper crust is characterized by a very high geothermal gradient of ~55
22 °C/km, evolving from greenschist to amphibolite facies, while the middle crust, exposed in a
23 gneissic core, exhibits granulite facies conditions with a near isothermal geothermal gradient
24 (<8°C/km) between 740 and 790°C.

25 The abnormal and discontinuous crustal geothermal gradient, dated at *c.* 305 Ma on syn-granulitic
26 monazite by LA-ICPMS, is interpreted to be the result of magmatic intrusions at different structural
27 levels in the crust: the Ansignan charnockite (*c.* 305 Ma) in the deepest part of the gneissic core, the
28 Tournefort granodiorite (*c.* 308 Ma) at the interface between the gneissic core and the upper crust
29 and the Saint-Arnac granite (*c.* 304 Ma) in the upper section of the massif. The heat input from
30 these magmas combined with the thermal buffering effect of the biotite dehydration-melting
31 reaction resulted in the near-isothermal geothermal gradient in the gneissic core (melt-enhanced
32 geotherm). The higher geothermal gradient (> 50°C/km) in the upper crust is only due to
33 conduction between the hot middle crust and the Earth's surface.

34 The estimated maximum finite pressure range suggests that about 10 to 12 km of crust are exposed
35 in the Agly massif while the present day thickness does not exceed 5 to 6 km. This pressure / depth

36 gap is consistent with the presence of several normal mylonitic shear zones that could have
37 contributed to the subtraction of about 5 km of the rock pile. Monazite U-Th-Pb ages carried out on
38 monazite overgrowths from a highly mylonitized sample suggest that this vertical thinning of the
39 massif occurred at *c.* 296-300 Ma.

40 This later Variscan extension might have slightly perturbed the 305 Ma geothermal gradient,
41 resulting in an apparent higher conductive geothermal gradient in the upper crust. Although the
42 Agly massif has been affected by Cretaceous extension and Eocene Alpine compression, we suggest
43 that most of the present-day thickness of the column rock was acquired by the end of the Paleozoic.

44

45

46

47

48 **1 INTRODUCTION**

49

50 Low pressure-high temperature metamorphism (LP-HT) in the continental crust is defined by high
51 geothermal gradient (60-150°C/km) and temperature reaching about 600-800 °C, at pressure below
52 0.4 GPa. These conditions are usually reached in contact metamorphism settings, resulting in
53 hornfels and possible partial melting of pelitic rocks close to the contact with the intrusive rocks.
54 Nevertheless, numerous examples for LP-HT metamorphic terranes have been ascribed to regional
55 metamorphic environments (De Yoreo, Lux, Guidotti, Decker, & Osberg, 1989; Kim & Cho, 2003
56 Gibson, 1991; Okay et al., 2013; Yardley, Barber, & Grey, 1987). Such high geothermal gradients,
57 much higher than steady state gradients for thickened crust, require a considerable heat flux to reach
58 such thermal state in the continental crust and are more common in Archean cratons (Brown, 2007;
59 2009). They have been commonly ascribed to crustal underplating of mantle-derived basic magma
60 (Thompson & England, 1984), intrusion of large felsic magma in the middle and upper crust (De
61 Yoreo et al., 1989; Lux, De Yoreo, Guidotti, & Decker, 1986) or Metamorphic Core Complexes
62 (Coney, 1980).

63 These regional LP-HT metamorphic gradients are commonly reported in gneissic domes and often
64 associated with magmatism and partial melting (De Yoreo et al., 1989; Kim & Cho, 2003). Over the
65 past decades, numerous studies have highlighted the important role of partial melting, thermal
66 buffering and advective heat transfer due to melt migration towards the structurally upper levels to
67 produce this particular thermal structure of the crust (Depine, Andronicos, & Phipps-Morgan, 2008;
68 Riel, Mercier, & Weinberg, 2016). One of the key feature of these studies is that the combined
69 effect of radioactive heat production, high mantle heat source, heat diffusion, latent heat of melting

70 and heat advection by melt transfer result in discontinuous thermal structure of the continental crust.
71 The upper crust is characterized by high to very high LP-HT geothermal gradient. In contrast the
72 middle to lower crust is partially molten and characterized by a low to very low geothermal
73 gradient. This thermal structure has been modeled and defined by Depine, Andronicos, & Phipps-
74 Morgan (2008) as a melt-enhanced geotherm. This discontinuous crustal thermal structure has been
75 described in various crustal settings including collisional setting, in the French Massif Central
76 (Trap, Roger, Cenko-Tok, & Paquette, 2016) and Himalaya (Groppo, Rolfo, & Indares, 2012), and
77 continental arc settings such as the Andean active margin in Ecuador (Riel et al., 2016).

78 Deciphering the thermal structure of the crust at a specific geological time (i.e. the geothermal
79 gradient) relies on the estimation of pressure and temperature conditions as well as dating peak
80 metamorphism for different rocks along a metamorphic field gradient-related cross-section.
81 Unfortunately, this task is not straightforward due to potential kinetics effect for amphibolite facies
82 rocks that makes part of the upper crust. Indeed, estimated peak temperature from equilibrium
83 thermodynamic modeling of phase relation may not reflect the “real” temperature because of kinetic
84 factors that delay the onset of nucleation and growth of metamorphic phases (Carlson, Pattison, &
85 Caddick, 2015; Pattison & Tinkham, 2009; Waters & Lovegrove, 2002). Additionally, field
86 metamorphic gradient may not be only the result of heat transport but could also be modified by
87 deformation processes. Heterogeneous deformation leads to low strain domains preserving relict
88 and metastable assemblages partially re-equilibrated while high strain domains are fully re-
89 equilibrated. Localized crustal shear zones can also modify metamorphic gradient by juxtaposing
90 terrains of different grades, disrupting the observed metamorphic gradient and leading to transient
91 geotherms.

92 LP-HT metamorphism is a common feature in the Variscan belt, especially in Pyrenean massifs: St
93 Barthélémy (Saint Blanquat, Lardeaux, & Brunel, 1990; Saint Blanquat, 1993), Canigou (Gibson,
94 1991), Aston-Hospitalet (Barnolas & Chiron, 1996; Denèle, Olivier, Gleizes, & Barbey, 2007). This
95 LP-HT metamorphism is usually associated with the development of gneissic domes and a
96 widespread late Variscan magmatism between 300-320 Ma (Cochelin et al. 2017, ref therein).

97 Different geodynamic models have been proposed that might be responsible for the LP-HT
98 gradients: (1) early extension with thinning during continental rifting associated with mantle-
99 derived magmas (Wickham & Oxburgh, 1985; Wickham, Oxburgh, Reading, & Vissers, 1987), (2)
100 late extension after crustal thickening (Van den Eeckhout & Zwart, 1988) or (3) compressional
101 setting with thickening associated with numerous intrusions in the crust and partial melting (De
102 Yoreo et al., 1989; Lux et al., 1986).

103 In the easternmost part of the French Pyrenees, the Agly massif is one of these gneiss domes that
104 preserves a complex HT-LP late Variscan tectono-metamorphic evolution (figure 1a). However, its

105 present-day geometry is not only due to Variscan tectonics but also results from the superposition of
106 late Cretaceous extension and Eocene Alpine compression (Clerc & Lagabrielle, 2014; Vauchez et
107 al., 2013). The late Variscan metamorphism event is characterized by a high geothermal gradient in
108 the upper crust of about 80 to 100°C/km (Fonteilles, 1976; Guitard, Vielzeuf, & Martinez, 1996;
109 Vielzeuf 1984) and up to 150°C/km in some localities (Delay, 1989), partial melting in the middle
110 crust and different generations of magmatic intrusions (Delay, 1990; Fonteilles, 1976; Guitard et al.,
111 1996). A detailed review of the bibliography reveals that quantitative thermobarometry has never
112 been published on the metamorphic gradient of the whole Neoproterozoic-Paleozoic sequence.
113 Furthermore, the available P-T estimations are restricted to the gneissic core, and mostly to the
114 deepest part near the Ansignan charnockite.

115 This paper is aimed at defining quantitatively the P-T conditions along the metamorphic gradient,
116 the age and thermal structure of the Agly massif during the Late-Variscan orogeny. A suite of
117 samples located at different structural levels were collected along an E-W cross section to constrain
118 peak P-T conditions via phase relation forward modeling. Two distinct lithologies have been used:
119 Ordovician pelites from the upper crustal level and Proterozoic pelites (kinzigites) from the gneissic
120 core, in order to minimize uncertainties on thermobarometric estimates and highlight possible
121 metamorphic discontinuities along the metamorphic gradient. In-situ LA-ICPMS U-Th-Pb monazite
122 dating has been used to constrain the timing of peak metamorphism and compared to previously
123 documented magmatic ages. Finally, we will discuss and propose a conceptual model taking into
124 account the role of partial melting, heat advection during magmatism and localized deformation
125 responsible for the finite shape of the HT-LP discontinuous Variscan geotherm.

126

127

128 **2 GEOLOGICAL SETTING**

129

130 **2.1 The Agly massif in the Pyrenees**

131

132 The Pyrenees mountain belt was formed during the Tertiary collision of the Iberian microplate and
133 the Eurasian plate (e.g. Choukroune, 1992). The Axial and Northern Pyrenean zones are
134 characterized by a suite of exhumed Variscan massifs (e.g. Aston, Hospitalet, Canigou, Trois-
135 Seigneurs, Agly), that consist of metasediments, para- and orthogneisses, migmatites and plutonic
136 rocks, thrust and juxtaposed to Mesozoic and Cenozoic covers.

137 The Agly massif is the easternmost Variscan massif of the Northern Pyrenean Zone in France
138 (Figure 1a). The southern boundary of the massif is an alpine NW-SE-trending and vertical fault

139 (Bélesta-Trilla fault) that brings into contact Variscan magmatic and metamorphic rocks with the
140 Boucheville syncline, consisting of Mesozoic sedimentary rocks (up to Albian) metamorphosed at
141 high temperature during Cretaceous time (~95 Ma) (Delay, 1990 and references therein). On its
142 northwestern edge, the Variscan Agly massif is locally thrust northward over the Mesozoic cover
143 (Triassic formation) of the Saint-Paul de Fenouillet syncline (Figure 1). In contrast, the same
144 contact towards the northeast has been recently interpreted as a detachment fault that juxtaposed the
145 Agly massif with the Mesozoic Agly syncline that has been metamorphosed during Cretaceous time
146 (Vauchez et al., 2013). Although it is well acknowledged that both northern contacts have been
147 tectonically reactivated during the Tertiary orogeny, there is a controversy about the age of this
148 extensional tectonic history that could be either Paleozoic or Cretaceous (Vauchez et al., 2013;
149 Olivier, 2013). This controversy has been rejuvenated by two recent studies using (U-Th)/He
150 (Ternois et al., 2019) and U-Pb (Odlum & Stockli, 2019) in both zircon and apatite. The first study
151 concluded that the Agly massif acquired most of its present-day geometry during Paleozoic times
152 while the second argued that most of the thinning occurred during pre-Alpine hyper-extension.
153 Distinct geodynamic models have been proposed to account for these structural, metamorphic and
154 magmatic features. Bouhallier, Choukroune, and Ballèvre (1991) proposed a late Variscan
155 extensional setting after crustal thickening, while Paquet and Mansy (1991) rather suggested that
156 crustal thinning may have occurred during Cretaceous time. On the other hand, Delay (1990) argued
157 for a late Variscan compressional setting with heat provided by a charnockitic intrusion in the lower
158 part of the massif. More recently, a bulk compression tectonics associated with a transpressive
159 setting has been proposed to explain the structural evolution of the Agly massif (Olivier, Gleizes, &
160 Paquette, 2004; Olivier, Gleizes, Paquette, & Muñoz Saez, 2008). It appears from this review that
161 there is no consensus on the geodynamic model, and this situation may have arisen partly because
162 the geothermal gradient (thermal structure) and the age of metamorphic and deformation events
163 have not been well constrained.

164

165 **2.2 Lithological units**

166

167 Since the pioneer work of Fonteilles and Guitard (1964) and Fonteilles (1970; 1976), the Variscan
168 Agly massif has been subdivided into two main units: (1) A metamorphosed Paleozoic sequence,
169 mostly exposed in the northeastern part of the massif with a thickness of ~2.5 to 3 km, that
170 structurally overlies (2) a high grade gneissic core of presumed late Proterozoic age in the
171 southwestern part of this area. Both units are intruded by Variscan to late Variscan plutonic bodies
172 (Ansignan charnockite, Tournefort diorite and the Saint-Arnac granite). The two main units were

173 classically interpreted as a sedimentary cover on top of an older basement, respectively (Fonteilles
174 & Guitard, 1964), but this interpretation is revised in this contribution.

175 The upper part of the Paleozoic sequence consists of Devonian limestones with minor and
176 discontinuous Silurian black phyllites and locally Late Ordovician (Caradoc) volcano-clastic rocks.
177 The lower part of the sequence is a monotonous and thick succession composed of an alternation of
178 siltstone and sandstone layers (Jujols group of Laumonier (1998)). Recent biostratigraphic age data
179 obtained on comparable rocks, on the southern slope of the Canigou massif (in the Pyrenean Axial
180 Zone, south of the Agly massif), suggest that the Jujols group may be of Late Cambrian - Early
181 Ordovician age and that most of the Early to Middle Ordovician sequence was eroded prior to the
182 deposition of the Late Ordovician volcano-clastic rocks during the Sarde tectonic event (Casas &
183 Palacios, 2012). The entire Paleozoic sequence has been affected by a low pressure-high
184 temperature (LP-HT) metamorphism that increases downward from lower greenschist facies
185 conditions at the top, leading to the transformation of Devonian and Silurian rocks into marbles and
186 calc-schists, respectively, to upper amphibolite facies conditions with partial melting involved, at
187 the bottom of the Jujols group (Fonteilles, 1970).

188 The "high grade gneissic core" is heterogeneous and consists of partially-melted metapelites
189 (locally garnet-cordierite-sillimanite-bearing gneiss) and metagreywackes interbedded with
190 discontinuous and highly deformed layers of calc-silicate gneisses and marbles. These meta-
191 sedimentary are inter-layered with orthogneisses of variable thickness (on the order of meters)
192 which were emplaced as granitic sills during Early Cambrian at *c.* 530-540 Ma (Tournaire Guille,
193 Olivier, Paquette, Bosse, & Guillaume, 2019). In the western part of the massif, the uppermost part
194 of the gneissic core is intruded by the kilometer thick Riverolles orthogneiss. The "gneissic core" is
195 separated from the Paleozoic Jujols group by a discontinuous intercalation of white metacarbonate
196 (the so-called "base marble"), which in some cases is present few meters inside the gneisses. All
197 these observations suggest that the metasediments of the "gneissic core" of the Agly massif are a
198 highly metamorphosed equivalent to the Late Neoproterozoic sediments of the Canaveilles group,
199 observed for instance south of the Agly massif, in the Canigou dome (e.g. Cocherie et al., 2005;
200 Laumonier, 1998). The Late Neoproterozoic age of the sediments was first suggested by Autran,
201 Fonteilles, & Guitard (1966) and Vitrac-Michard and Allegre (1975), but they argued for a cover
202 and pre-Variscan basement relationships (see review in Padel, 2016).

203 The Paleozoic sequence (Jujols group) and the gneissic core (Canaveilles group) were intruded by
204 late Variscan plutons. In the southwestern part of the massif, the deepest part of the gneissic core
205 was intruded by the Ansignan charnockite. This intrusion is a 500 to 800 m thick laccolith parallel
206 to slightly discordant to the main foliation and consists of an orthopyroxene-bearing granodiorite
207 with megacrysts of K-feldspar defining an internal magmatic foliation. The age of magmatic

208 emplacement of this intrusion was initially constrained at 314 ± 6 Ma by Respaut and Lancelot
209 (1983) on monazite grains, and more recently re-evaluated at 307 ± 3 Ma (Tournaire Guille et al.,
210 2019) on zircons. The upper part of the gneissic core was intruded by the meter-thick Cassagnes
211 sills at the same time (308 ± 3 Ma, Tournaire Guille et al., 2019), and may be equivalent to the
212 Ansignan intrusion except that it is orthopyroxene-free and was emplaced in an upper structural
213 level. In the northwestern part of the Agly massif, the Paleozoic sequence was intruded by the late
214 Variscan Tournefort Diorite and the Saint-Arnac granite at 308 ± 1 Ma and 304 ± 5 Ma,
215 respectively (Olivier et al., 2008). While the Tournefort diorite was emplaced at the base of the
216 Jujols Group sequence, the Saint-Arnac granite intruded the entire Jujols group. Emplacement of
217 the late Variscan Tournefort diorite and Saint-Arnac granite induced a local contact metamorphism
218 with the development of partial melting around the diorite and late muscovite crystallization around
219 the granite contact and in the metasediment septas present in the granite.

220

221 **2.3 Tectono-metamorphic evolution**

222

223 The Paleozoic sequence shows a progressive downward increase of metamorphic conditions, with
224 the following succession of isograds: chlorite out, biotite in, cordierite in, andalusite in, sillimanite
225 in, muscovite out and finally water saturated partial melting. Based on semi-quantitative phase
226 diagram projections and the estimation of the thickness of the Paleozoic sequence, the late-Variscan
227 geothermal gradient has been estimated between 130 and 150 °C·km⁻¹ (Fonteilles, 1970) or at 80
228 °C·km⁻¹ (Delay, 1990).

229 The gneissic core recorded a more homogenous upper amphibolite to granulite facies conditions of
230 metamorphism. Nevertheless, the gneissic core is classically divided into two structural levels based
231 on their metamorphic assemblages (Fonteilles, 1970): the Belesta gneisses forming the upper part
232 with K-feldspar-sillimanite-bearing assemblages, and the Caramany gneisses in the deepest part
233 with orthopyroxene-bearing assemblages. Metamorphic conditions estimated on the Ansignan
234 charnockite or nearby lithologies have been estimated at 0.6 ± 0.1 GPa and 750 ± 50 °C (Andrieux,
235 1982), 0.5 ± 0.05 GPa and 800 ± 100 °C (Vielzeuf, 1984) or 0.4 ± 0.05 GPa and $600-650$ °C
236 (Delay, 1990).

237

238 **2.4 Deformation**

239

240 The metamorphic rocks of the upper Paleozoic sequence and the lower gneissic core share a
241 predominant strain fabric observed in the entire Agly massif that corresponds to a moderately to

242 shallowly dipping HT/LP foliation, holding a conspicuous N20 trending mineral and stretching
243 lineation (e.g. Bouhallier et al., 1991; Olivier et al., 2004). Similarly, the Ansignan charnockite and
244 the Cassagnes intrusives show a well-developed magmatic foliation, with a minor component of
245 solid-state deformation. This magmatic foliation is parallel to the main LP/HT foliation of the
246 surrounding gneisses (Delay, 1989; Olivier et al., 2004).

247 In addition to the main foliation, the gneissic core is characterized by the development of low angle
248 extensional mylonitic shear zones, mainly visible in the eastern part of the massif, dipping either
249 toward the north or toward the south and associated with a strong stretching lineation that trends
250 N20 (Delay, 1989). The main foliation and the mylonitic shear zones show a similar normal and
251 top-to-the north kinematics attributed to a same tectono-metamorphic event responsible for the
252 thinning of the Variscan crust (Vanardois et al. in press). Olivier et al. (2004; 2008) suggest a local
253 thinning during a late Variscan transpressive regime with the mylonitic normal shear zones that
254 developed in response to late doming. In contrast, Bouhallier et al. (1991) documented a major
255 detachment zone located between the Paleozoic sequence and the gneissic core (the Caladroy-
256 Latour shear zone) that would be responsible for the subtraction of about 10 km of crustal material
257 and consequently the juxtaposition of the low pressure-medium temperature Paleozoic sequence
258 with the moderate pressure-high temperature gneissic core. The age of mylonitic shearing (either in
259 a context of crustal thinning or transpression) is still a matter of debate. For Delay (1990) and
260 Bouhallier et al. (1991), the extension is contemporaneous with the HT-LP metamorphism and
261 therefore would be late Variscan (*c.* 315 Ma). On the contrary, Olivier et al. (2008) argued that the
262 root of the ~304 Ma Saint-Arnac and Tournefort plutonic body underwent northward normal
263 shearing suggesting that the development of mylonitic shear zones took place just after 304 Ma. In
264 contrast, Paquet & Mansy (1991) suggested that the thinning responsible for the loss of ~ 10 km of
265 crustal material occurred during Mid-Cretaceous time (110-100 Ma).

266 The E-W trending fault that bounds the southern limb of the Mesozoic Agly syncline (north-eastern
267 part of the Agly massif) has recently been interpreted as an ancient Mid-Cretaceous detachment
268 fault (~100 Ma), with a top-to-the-north shearing sense (Vauchez et al., 2013). This contact may
269 have contributed to the exhumation of the Agly massif during the Iberian microplate rotation
270 relative to Eurasia and opening of the Bay of Biscay during or after Albian (Vauchez et al., 2013).
271 Vauchez et al. (2013) also suggested that some of the extensional mylonitic shear zones observed in
272 the Variscan basement, and described above, may also be related to this Mid-Cretaceous
273 extensional event. Furthermore, this Mid-Cretaceous deformation is coeval with an intense episode
274 of fluid circulation and fluid-rock interactions that are responsible for the local albitization of the
275 Saint-Arnac granite, the paragneisses of the gneissic core and, locally, the Paleozoic sequence
276 (Poujol, Boulvais, & Košler, 2010).

277 Most of the tectonic contacts bounding the Agly massif to the north and the south have been
278 reworked during the Tertiary orogeny corresponding to the N-S convergence between Iberia and
279 Eurasia during Eocene time. For instance, the reactivation of the western part of the upper
280 Cretaceous detachment, described above, corresponds to the northward thrusting of the Agly massif
281 over the Mesozoic cover of the Saint-Paul de Fenouillet syncline (Figure 1). Alpine deformation is
282 also visible within the Agly massif where Mesozoic carbonate cover and Early Eocene Breccias are
283 pinched into the high-grade rocks between steeply dipping N110 trending Alpine faults (Figure 1b).
284

285

286 **3 METAMORPHIC GRADIENT ESTIMATION**

287

288 As introduced in the previous section, the N20 pervasive foliation of the main metamorphic event
289 (LP/HT) defines a single tectono-metamorphic event throughout the entire massif that can be linked
290 to the Charnockite emplacement at 305 Ma. This lineation is similar to the stretching lineation of all
291 mylonitic shear zones. Thus, sampling along the metamorphic gradient should be in a N-S direction
292 in order to highlight the possible role of mylonitic shear zones on the finite metamorphic gradient
293 shape. However, the occurrence of major East-West trending post-Mesozoic steep faults and
294 Pyrenean thrusts that may have juxtaposed blocks of different structural level precludes a simple
295 north-south sampling. Furthermore, in the central part of the Agly massif, where the deepest part
296 located around the Ansignan charnockite is exposed, the metamorphic gradient in the Paleozoic
297 sequence is obliterated by the St Arnac granitic intrusion. For these reasons, we have chosen to
298 sample the different structural levels along an E-W cross section (Figure 2), from Força Real on the
299 Eastern side of the massif, towards the lowest structural levels near the Ansignan charnockite on the
300 western side. The location of this cross section is represented on the map (Figure 1b). The GPS
301 coordinates for each sample can be found in Table 1.

302 **3.1 Petrology**

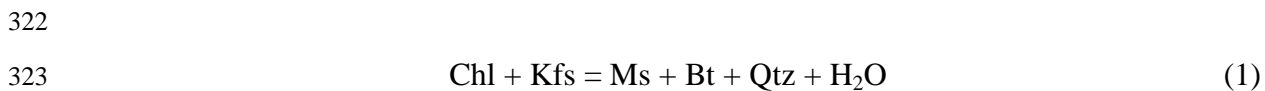
303 **3.1.1 Metamorphic evolution of the Late Cambrian - Early Ordovician** 304 **sequence (Jujol group)**

305 The Agly massif preserves a typical LP-HT metamorphic gradient in the cover as suggested in
306 previous studies (Fonteilles, 1970; Guitard et al., 1996; Vielzeuf, 1984) and referred to here as the
307 upper Paleozoic sequence (Jujol group). The sequence of mineral isograds is biotite-in, closely
308 followed by chlorite-out, cordierite-in, andalusite-in, sillimanite-in, muscovite-out/K-feldspar-in

309 and onset of partial melting. We describe here the different reactions that could lead to the
310 appearance and disappearance of these index minerals based on the petrography and available
311 petrogenetic grids (Pattison & Tracy, 1991; Spear & Cheney, 1989). For clarity, all reactions are
312 represented in the simplified KFMASH system. Consequently, the role of plagioclase and other Ca-
313 bearing phases is not taken into account to describe the main phase transitions.

314 The first observable isograd of the LP-HT metamorphic gradient is the biotite-in. This reaction
315 results in the appearance of small biotite flakes in the fine-grained chlorite-muscovite bearing
316 schists. Biotite content continuously increases with increasing metamorphic grade. The low-grade
317 chlorite-muscovite schists preserve evidences of a bedding that corresponds to an alternation of
318 millimeter to centimeter thick phyllosilicates-rich and quartz-rich layers (Figure 3a).

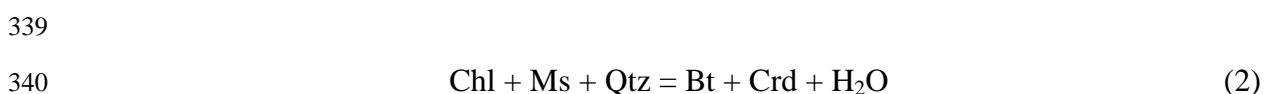
319 The very fine-grained nature of the chlorite schists makes difficult the petrographic observation, and
320 although we have not observed K-feldspar, we suggest that the first appearance of biotite is the
321 result of the simplified reaction:



325 This reaction is consistent with the observation of micro-lithons bearing chlorite and surrounding
326 preferred orientation of muscovite and biotite parallel to the HT/LP foliation (caption Figure 3a, see
327 S cleavage).

328 In the field, the continuous increase of biotite content results in a striking change in color and grain
329 size from a greenish and very fine-grained chlorite-muscovite schist to a darker and coarser biotite-
330 muscovite schist (Figure 3b). The darker color is mostly due to the presence of graphite derived
331 from organic matter, present until partial melting.

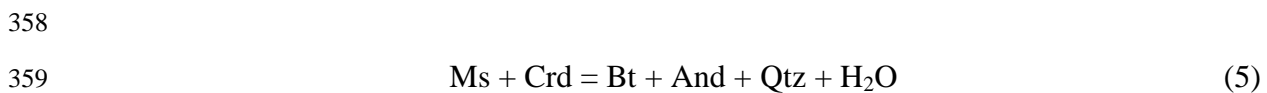
332 The next isograd corresponds to the appearance of cordierite porphyroblasts together with the
333 complete disappearance of primary chlorite (Figure 3c). This isograd is immediately followed by
334 the appearance of andalusite in the stability field of cordierite. Preferred orientation of cordierite
335 and andalusite porphyroblasts underline the orientation of the main N20 stretching lineation. In
336 high-aluminum pelites, several chlorite dehydration reactions can be responsible for the
337 crystallization of cordierite at low pressure. All of them involve muscovite, chlorite and quartz as
338 reactant phases and biotite and H₂O as products:



343

344 Based on field observations, cordierite appears before andalusite. This together with the pattern of
345 inclusions inside andalusite visible in figure 3d (i.e. only biotite and quartz without core to rim
346 differences) suggest that cordierite grew outside the stability field of andalusite due to reaction (2).
347 Nevertheless, this interpretation would require a more Mg-rich bulk composition. Several factors
348 can explain this compositional discrepancy. Measured bulk X_{Mg} composition varies from ~ 0.4 to
349 0.5 (see AFM diagram figure 4), which is very close to both chlorite and biotite that are close to 0.5
350 in X_{Mg} . Thus, small retrograde changes in X_{Mg} of these phases can potentially override the prograde
351 compositions and make interpretations based on AFM more difficult. Additionally, iron-sulfide is
352 usually present in such rocks, but bulk rock composition was not projected since no major element
353 of oxides were constrained. This would change the X_{Mg} of the equilibrium volume considered, and
354 most likely would be a function of temperature since iron sulfides usually vary along the pyrite-
355 pyrrhotite join.

356 The pattern of inclusions inside andalusite together with the progressive disappearance of cordierite
357 in the stability field of andalusite is interpreted as the consequence of the reaction:



360
361 The next encountered isograd is the appearance of fibrolitic sillimanite (Figure 3e), that forms
362 millimeter-size nodules elongated within the main stretching direction. In one sample, we found
363 evidence of polymorphic breakdown of andalusite into sillimanite (reaction 6), having the two
364 minerals coexisting but never in direct contact as observed by many authors (e.g. Carmichael,
365 1969). However, the sillimanite isograd mapped in the field rather corresponds to the muscovite
366 breakdown reaction (reaction 7) that produced large cluster of fibrolite, which are easier to observe
367 in the field.



371
372 The last observed isograd in the upper Paleozoic sequence corresponds to the onset of partial
373 melting that is characterized by the formation of quartzo-feldspatic leucosomes parallel to the
374 HT/LP main foliation (Figure 3f). In the field, the melt-in isograd is always located a few tens of
375 meter away from the muscovite-out isograd that corresponds to reaction (7). Onset of partial
376 melting is assumed to be water saturated or near water saturation. Partially molten micashists host
377 tourmaline-bearing pegmatitic bodies that range in thickness from a few centimeters up to a several
378 decameters. In the vicinity of these pegmatites, the micashists are characterized by the

379 crystallization of late euhedral muscovite that cross-cut the main foliation (Ms2 in figure 3e).
380 In the field, the thickness of the partially molten micaschist zone represents only a few decameters
381 to a hundred meters. Then the molten micaschists evolve into a biotite-rich quartzo-feldspathic
382 gneiss characterized by minute porphyroblast of K-feldspar. This lithology has been referred by
383 Delay (1990) as the “pearled gneiss”. Partial melting evidences in this lithology are rare and when
384 present consist of discrete dismembered leucosomes. We suggest that the onset of partial melting
385 resulted in a strong fractionation of water into the melt leading to local fluid-undersaturation and
386 therefore subsolidus conditions. Furthermore, in most locations, including Caladroy, the “pearled
387 gneiss” is strongly deformed and consists in mylonitized partial melted micaschists. Bouhallier et.
388 al (1991) described a high strain zone in Caladroy having an abrupt transition between the
389 micaschists and the gneisses. The transition between micaschists and pearled gneisses is also
390 characterized by a discontinuous intercalation of a marble layer, the so-called “base marble”, that
391 can be located either at the interface between the partially molten micaschists and the gneiss or
392 within the gneiss itself. To conclude, we propose that the “pearled gneiss” is derived from the same
393 Early Ordovician protolith as the overlying micaschist and schist, and is produced by concomitant
394 water-undersaturated metamorphism and strain localization.

395

396

397 **3.1.2 Kinzigites of the gneissic core**

398 The gneissic core, located structurally below the metamorphosed upper Paleozoic sequence (Jujol
399 group), is mainly composed of paragneisses, orthogneisses and metacarbonates, the latter being
400 more abundantly present in the deeper part of the massif (Figure 2). In this study, we have chosen to
401 focus our petrological analysis on kinzigites (bt-sil-crd-grt bearing gneisses) that occur as
402 discontinuous meter-scale layers at different structural levels in the gneissic core (Figure 2). These
403 rocks are good candidates for calibrating P-T peak conditions across the entire gneissic core using
404 P-T pseudosections. The studied samples show the same peak metamorphic mineralogical
405 assemblage that consists of cordierite + garnet + sillimanite + biotite + alkali feldspar + quartz ±
406 plagioclase (see samples 10Ag04, 10Ag11 and 11Ag03, Figure 4). Sillimanite occurs either as
407 elongated prismatic grains, which define, with biotite, the main foliation wrapping around garnet
408 and cordierite porphyroblasts (Figure 4a), or small needle inclusions in garnet, together with quartz
409 and biotite; sillimanite commonly exhibits both textural positions in the same sample. Although
410 evidences of partial melting are unclear at the thin-section scale due to post-peak deformation, field
411 observations clearly suggest that these rocks were partially molten. All these minerals are stable at
412 peak metamorphic conditions, and are consistent with biotite dehydration melting reaction:

413

414
$$\text{Bt} + \text{Sil} + \text{Qtz} = \text{Grt} + \text{Crd} + \text{Kfs} + \text{H}_2\text{O} \text{ or } \text{L} \quad (8)$$

415

416 Some studied kinzigites also show late shear zones where a high-temperature retrogression
417 assemblage of Bi + Sill is observed. Samples 10Ag04, located near the Trilla bridge, shows that the
418 peak metamorphic assemblage is partially overprinted by brittle deformation that results in the
419 cataclasis of garnet porphyroblasts (Figure 4b). Similarly, sample 11Ag03, near the Cuxous castle,
420 is affected by numerous extensive ductile to brittle-ductile shear zones without low-temperature
421 retrogression, except for a strong retrogression of cordierite and K-feldspar (Figure 4c).

422

423

424 **4 THERMOBAROMETRY**

425

426 To constrain the P-T conditions along the metamorphic gradient, pseudosections were
427 computed using two thermodynamic modelling programs, Perple_X (Connolly & Petrini, 2002,
428 Connolly, 2005) and Domino/Theriak (De Capitani & Petrakakis, 2010). Whole rock analyses are
429 from XRF analyses and are presented in table 1. Since no mineral zoning and very limited
430 retrogression was observed, the bulk rock XRF analyses represent a good estimate of the
431 equilibrium volume for both the HT-LP rocks and the rocks from the gneissic core.

432

433 **4.1.1 Late Cambrian – Early Ordovician LP-HT gradient**

434 In the case of the Late Cambrian - Early Ordovician sequence, the bulk chemistry is rather
435 homogeneous (Figure 5). The effect of bulk composition variability on phase relations and the
436 location of major phase boundaries are thus very limited (Figure 5b). Therefore, phase relations
437 were computed with the bulk composition of sample 10Ag16, in the middle of the sample
438 composition cluster (white dot, Figure 4). The P-T phase diagram section produced in
439 NCKFMASHT (Figure 6a) shares similarities with the P-T projection (petrogenetic grid) of
440 Pattison & Tracy (1991) that was used by Guitard et al. (1996) to constrain semi-quantitatively the
441 LP-HT metamorphic gradient in the Agly massif for the first time. In this contribution we
442 rejuvenate this approach quantitatively with more petrological constraints and using recent
443 thermodynamic databases.

444 Figures 6b, c and 7 show that the metamorphic P-T conditions are bracketed in a temperature range
445 from 500-520°C (chlorite breakdown, reaction (2) outside the stability field of andalusite) to 660-

446 680°C (muscovite breakdown, reaction (7) and the onset of partial melting at ~ 0.35 GPa.
447 Defining the exact temperature (and pressure) of intermediate samples characterized by the
448 appearance of andalusite and cordierite is more challenging because of the controversy regarding
449 the exact P-T slope and location of reaction (5) that involves both andalusite and cordierite. In the
450 computed NCKFMASHT phase diagram section (Figure 6a), the positive slope of the reaction (5),
451 here represented by the field Ms + Crd + Bt + And + Qtz + Pl + Ilm (labelled “Ms Crd Bt And” in
452 figure 6a), is in contradiction with field observations made in many low pressure contact aureoles as
453 well as the Agly massif, where cordierite appears just before andalusite (Pattison, Spear, Debuhr,
454 Cheney, & Guidotti, 2002; Pattison & Vogl, 2005; Pattison & Debuhr, 2015). As can be seen in
455 figure 6b, this inconsistency is not related to bulk compositional variations, although the position of
456 this equilibrium varies with X_{Mg} bulk rock composition.

457 The reaction 5 has low entropy change, thus it is very sensitive to the quality of the thermodynamic
458 data. To overcome this known problem in low pressure metapelites, Pattison & Debuhr (2015) used
459 a modified Berman (1988) thermodynamic database (Pattison et al. 2002; Pattison & Debuhr, 2015;
460 Spear & Cheney, 1989; Spear & Pyle, 2010) instead of the Holland and Powell (1998) or (2011)
461 version; this database is referred to here as SPaC14 as in Pattison & Debuhr (2015). Their approach
462 was (1) to simplify the chemical system (excluding non-essential components like Na₂O, CaO and
463 TiO₂) to minimize uncertainties related to poorly constrained thermodynamic constant of pure end-
464 member, and (2) to use simplified ideal site mixing solid-solutions. Following this approach, we
465 have computed the phase diagram section in a simplified KFMASH system shown in figures 6c and
466 6d using the 1998 version of the Holland and Powell thermodynamic database, updated in 2002,
467 and the SPaC14 database, respectively. The bulk composition used is the same as in figure 6a,
468 except that Na is projected through albite, Ca through anorthite and Ti through ilmenite, resulting in
469 a small variation in the molar amount of Al₂O₃, SiO₂ and FeO contents of the equilibrium volume
470 considered in the KFMASH system. As shown by Pattison & Debuhr (2015), the use of the SPaC14
471 database results in a phase diagram with a negative slope for the Crd + And + Bt + Ms equilibria
472 (5), that is more consistent with the appearance of cordierite and then andalusite along a prograde
473 path at ~ 0.3 GPa. In figures 6c and 6d, it is interesting to note that andalusite is predicted to be
474 stable at low temperature in equilibrium with chlorite and chloritoid (i.e. before the appearance of
475 cordierite). This feature is commonly described in contact aureoles, for example in the Bugaboo
476 aureole (Pattison & Debuhr, 2015) or the Little Cottonwood (Wohlert & Baumgartner, 2012), but is
477 in contradiction with field observations in the Agly massif. In the case of the Agly massif, we
478 suggest that the stabilization of andalusite and chloritoid is the result of excess aluminum in the
479 calculated bulk composition after albite and/or anorthite projection. At these P-T conditions,
480 paragonite is very likely to be stable but it is not taking into account in this modeling, resulting in a

481 higher Al₂O₃ content of the effective bulk composition.

482 The main petrological constrains for the metamorphic gradient of the Paleozoic sequence are: 1)
483 chlorite breakdown and crystallization of biotite and cordierite, 2) crystallization of andalusite with
484 or without cordierite present, 3) andalusite/sillimanite polymorphic transformation, 4) muscovite
485 breakdown without cordierite stable, and 5) melting outside the stability field of muscovite.
486 Minimum pressure in the low-temperature side of the gradient (~550 °C) cannot be constrain using
487 solely the phase diagram. However, the thickness of rocks above the Paleozoic schists is inferred to
488 be approximatively 10 km (Olivier et al. 2004). Assuming a density of the crust of 2.7 g/cm³ would
489 give a pressure around 0.27 GPa. The transition from andalusite to sillimanite, breakdown of
490 muscovite and partial melting occur on a very short distance in the field and a very limited
491 temperature range (620 to 670 °C) suggest that the maximum pressure is limited by the location of
492 the invariant point (i) at 0.35 GPa. Assuming a linear gradient, these two values (0.27 GPa at 550
493 °C and 0.35 GPa at 670 °C, allow us estimating the gradient at 55°C/km (2076 °C/GPa with 2.7
494 g/cm³). Such value is in very good agreement with a conductive gradient between partially molten
495 schists at 670 °C and 0.35 GPa (i.e. a 13 km depth), and the surface since the resulting gradient
496 would be ~52 °C/km. This high value is however lower than the previous qualitative estimates of 80
497 to 100 °C/km (Fonteilles, 1976; Delay, 1989; Guitard et al., 1996; Vielzeuf 1984).

498

499

500 **4.1.2 Kinzigites from the gneissic core**

501 To constrain the P-T conditions in the gneissic core, we have selected 10 kinzigite layers
502 from various structural levels. The pristine kinzigite samples preserve the same peak mineral
503 assemblage produced by biotite dehydration-melting reaction, which has a steep slope in P-T space
504 (Figure 8a). In addition, divalent cations composition of garnet was used to better constrain P-T
505 conditions and highlight continuous or discontinuous changes in pressure and temperature along the
506 cross-section. A phase diagram section was computed for each sample with Perple_X using whole
507 rock XRF composition. Garnet compositions were determined using electron microprobe with
508 wavelength dispersive spectrometry (WDS) during 3 sessions. The first two sessions were
509 conducted with a JEOL Superprobe 8200 at the Institute of Earth Sciences at the University of
510 Lausanne, the third session was on a Cameca SX100 at the University of Lille 1. Synthetic and
511 natural minerals were used for standardization. Average compositions and variations for the flat
512 core of garnets for each sample can be found in table 2, full analyses can be download with the
513 supplementary materials.

514 There is no discernable zonation at the level of precision of EPMA analyses (Figure 7),

515 except for small increase in Fe/(Fe + Mg) at the rim, due to retrograde interdiffusion with biotite.
516 Spessartine content can locally increase at the rim when garnet is retrogressed by biotite due to a
517 very high preference for incorporation of Mn in garnet compare to biotite (Kohn & Spear 2000).
518 The assumed equilibrium composition used to constrain P-T conditions were always coming from
519 garnet cores. Figure 8a is an example of pseudosection obtained for the sample 11Ag03. Almandine
520 and pyrope content in garnet are suitable to constrain P-T conditions because the slope of their
521 isopleths is either temperature or pressure dependent in the quadrivariant garnet – melt – bearing
522 stability fields located on both sides of the main equilibrium (8). There is generally a very good
523 agreement between almandine and pyrope compositions for all samples, with isopleths usually
524 located close from each other (Figure 8a). Spessartine and grossular content are very low, i.e. below
525 5 % of the X site of garnet, except for 4 samples (Table 2), thus they do not represent a good
526 constraint for P-T condition due to a limited accuracy of the thermodynamic database for these low
527 contents.

528 A synthesis of estimated P-T conditions is shown in figure 8c and shows a range in P-T
529 conditions from 0.49 GPa, 730°C to 0.65 GPa, 790°C. However, there is good agreement between
530 the pressure estimates from thermodynamic modelling and the relative structural position (i.e.
531 depth) of samples in the gneissic core (Figure 8c). Samples located in the upper part of the gneissic
532 core above the Ansignan charnockite intrusion have pressures ranging between 0.49 and 0.55 GPa
533 (Figure 8c). The minimum pressures of 0.50 to 0.52 GPa were obtained on samples 10Ag03,
534 10Ag09, 11Ag03 and 11Ag04 which are located a few tens to hundreds of meters below the sheared
535 contact with the Paleozoic sequence. The difference in pressure with the deepest sample from the
536 upper Paleozoic sequence (partially melted micaschist: 0.35 GPa at 670°C) is about 0.15 GPa.

537 Sample 10Ag11 located in the western central part of the massif and structurally in the
538 middle of the gneissic core gave P-T conditions of 0.57 GPa and 750°C. In contrast, samples
539 10Ag01 and 10Ag02 that are the deepest samples, below the Ansignan charnockite, are
540 characterized by pressures estimates of 0.66 and 0.62 GPa for temperatures of 770-800°C,
541 respectively. However, sample 10Ag04, that is also located below the charnockite and may belong
542 to the same kinzigite layer as 10Ag01 and 10Ag02, gave inconsistent pressure estimate of 0.52 GPa.
543 If we disregard sample 10Ag04, then the difference in pressure between samples located in the
544 deepest level and 10Ag11 is around 0.1 GPa (~2.7 km), which contrasts significantly with the
545 observed thickness on cross-section that does not exceed 200 m.

546

547

548

5 U-Th-Pb MONAZITE GEOCHRONOLOGY

549
550

551 5.1 Studied samples

552

553 Three kinzigites (10Ag02, 10Ag04 and 11Ag03) have been collected in order to constrain the
554 timing of metamorphism. These samples are located at different structural levels and show various
555 degree of deformation and retrogression. The deepest samples, 10Ag02 (Agly lake) and 10Ag04
556 (near the Trilla bridge), come from the same structural level (Figure 1 and 2). They are pristine
557 kinzigites that consist of garnet, cordierite, sillimanite, quartz and feldspar with minor biotite.
558 Sample 10Ag04 shows a more penetrative foliation with localized thin shear zones where garnet is
559 fractured and partially dismembered (Figure 9b). Sample 11Ag03 comes from the uppermost level
560 of the gneissic core, near the castle of Cuxous. It is characterized by the development of a mylonitic
561 foliation, normal shear sense ductile shear zones and brittle fractures that affect sillimanite and K-
562 feldspar porphyroclasts (Figure 9c). Peak metamorphic phases like K-feldspar and cordierite are
563 almost completely pinnitised in this last sample.

564

565 5.2 Analytical methods

566

567 In situ U-Th-Pb isotopic data were obtained by laser ablation inductively coupled plasma
568 spectrometry (LA-ICP-MS) at Laboratoire Magmas & Volcans (Clermont-Ferrand, France). The
569 analyses involved the ablation of minerals with a Resonetics Resolution M-50 powered by an ATL
570 Atlex Excimer laser system operating at a wavelength of 193 nm. For monazite, spot diameters of 9
571 μm were used, associated with repetition rate of 1 Hz and laser fluence of 9 J/cm^2 . The ablated
572 material was carried by helium and then mixed with nitrogen and argon before injection into the
573 plasma source of an Agilent 7500 cs ICP-MS equipped with a dual pumping system to enhance
574 sensitivity (Paquette et al., 2014). The alignment of the instrument and mass calibration were
575 performed before every analytical session using the NIST SRM 612 reference glass, by inspecting
576 the signal of ^{238}U and by minimising the ThO⁺/Th⁺ ratio (< 1%). The analytical method for isotope
577 dating is similar to that developed and reported in Paquette and Tiepolo (2007) and detailed in
578 Hurai et al. (2010) and Gasquet (2010). The signals of $^{204}(\text{Pb}+\text{Hg})$, ^{206}Pb , ^{207}Pb , ^{208}Pb , ^{232}Th and
579 ^{238}U masses were acquired. The occurrence of common Pb in the sample was monitored by the
580 evolution of the $^{204}(\text{Pb}+\text{Hg})$ signal intensity, but no common Pb correction was applied owing to the
581 large isobaric interference from Hg. The ^{235}U signal was calculated from ^{238}U on the basis of the
582 ratio $^{238}\text{U}/^{235}\text{U} = 137.88$. Single analyses consisted of 30 seconds of background integration with the

583 laser off, followed by 60 seconds integration with the laser firing and a 20 second delay to wash out
584 the previous sample and prepare for the next analysis.

585 Data were corrected for U-Pb fractionation occurring during laser sampling and for
586 instrumental mass discrimination (mass bias) by standard bracketing with repeated measurements of
587 the Trebilcock monazite (Tomascak et al., 1996) reference material. Repeated analyses of the
588 monazites Itambé and Bananeira (Gonçalves et al., 2016) reference materials, treated as an
589 unknown independently control the reproducibility and accuracy of the corrections. Data reduction
590 was carried out with the software package GLITTER® from Macquarie Research Ltd (Jackson et
591 al., 2004; van Achterbergh et al., 2001). For each analysis, the time resolved signals of single
592 isotopes and isotope ratios were monitored and carefully inspected to verify the presence of
593 perturbations related to inclusions, fractures, mixing of different age domains or common Pb.
594 Calculated ratios were exported and reported in $^{208}\text{Pb}/^{232}\text{Th}$ vs. $^{206}\text{Pb}/^{238}\text{U}$ “Concordia” diagrams
595 generated using the Isoplot/Ex v. 2.49 software package of Ludwig (2001). Owing to the lack of
596 correlation between Th/Pb and U/Pb uncertainties, a low correlation coefficient value of 0.1 was
597 considered in the calculations. The concentrations of U-Th-Pb were calibrated relative to the values
598 of the GJ-1 zircon (Jackson et al. 2004) and Trebilcock (Tomascak et al., 1996) reference materials.
599

600 5.3 Results

601 5.3.1 Pristine kinzigite from the gneissic core (10Ag02 and 10Ag 04)

602 Monazites in sample 10Ag02 (Agly lake) are located in the matrix and range in size from 20 to 100
603 μm . Two distinct compositional domains are defined based on Y distribution: a Y rich core and Y
604 poor rim (Figure 10a). Th and U content is constant between both domains. Six monazite grains
605 were analyzed and most of the analyses are concordant in a $^{232}\text{Th}/^{208}\text{Pb}$ vs $^{238}\text{U}/^{206}\text{Pb}$ concordia
606 diagram (table 3, Figures 10a and 11a). Y-rich cores give the oldest ages, with $^{232}\text{Th}/^{208}\text{Pb}$ ages
607 ranging from 240 ± 7 Ma to 311 ± 9 Ma. The four oldest analyses were selected to calculate a
608 concordant age at 305 ± 4 Ma ($\text{MSWD}_{(C+E)} = 1.5$). Y-poor rims show a spread of concordant ages
609 that range for *c.* 307 to 232 Ma, which precludes the calculation of concordant age (Figure 11a, red
610 circles).

611 Monazites in sample 10Ag04 are either present as inclusions in garnet or grains in the matrix. They
612 range in size from 50 to 150 μm (Figure 10b). Two compositional domains are defined based on Y
613 and Th/U compositions. Monazite included in garnet (m2 and m5) and the core of monazite in the
614 matrix (m3, m6, m8, m9) are characterized by high and variable Y content with a very constant
615 Th/U of 6.5 ± 1 (Table 3, Figure 10b). Monazite in the matrix are all characterized by small
616 overgrowths (10 to 20 μm) with very low Y content (m1, m3, m4, m6, m8, m9) and a very high and

617 variable Th/U, ranging from 10 to 34 (Table 3, Figure 10b). Grain m4 is homogeneous in
618 composition, with low Y content and high Th/U ratio, it is interpreted to belong to the same
619 generation as the overgrowths based on its composition. Monazite included in garnet do not show
620 low Y and high Th/U overgrowth suggesting that the formation of the overgrowths is post-garnet
621 crystallization and monazite entrapment. Eight monazite grains were dated. Seventeen isotopic
622 analyses belonging to the five monazites with high Y content and low Th/U ratio were performed.
623 On a $^{232}\text{Th}/^{208}\text{Pb}$ vs $^{238}\text{U}/^{206}\text{Pb}$ concordia diagram, all sixteen analytical points are concordant and
624 allow to calculate a concordia age of 306 ± 2 Ma ($\text{MSWD}_{(\text{C+E})} = 1.05$), which is consistent with the
625 concordia age obtained on 10Ag02 (Figure 11a and b). The constant Th/U ratio and the occurrence
626 of monazite included in garnet suggest that this age correspond to the age of the peak
627 metamorphism. The second compositional domain corresponding to the low Y and high Th/U
628 overgrowth, yield a second set of twelve concordant dates with a concordia age of 300 ± 2 Ma
629 ($\text{MSWD}_{(\text{C+E})} = 0.71$) (Figure 11d).

630

631 **5.3.2 Deformed kinzigite of the upper gneissic core (11Ag03)**

632 Five monazites located in the matrix were mapped. They range in size from 50 to 120 μm . Most of
633 the grains show homogeneous, large, Y-depleted core surrounded by an Y rich overgrowth that do
634 not exceed 10 μm in size (Figure 10c). Thorium content and distribution are homogeneous at the
635 grain scale. Monazite 1 differs from the others because it preserves an irregular very low Th core
636 (table 3 and Figure 10c). Three of the monazite grains analyzed (m1, m2 and m3, Figure 9c) show a
637 cluster of nine concordant dates that allow calculating a concordia age of 296 ± 2 Ma ($\text{MSWD}_{(\text{C+E})}$
638 $= 1.3$) (Figure 11c). A single analysis has been obtained on the Th poor core of monazite 1 (#16d:
639 $^{232}\text{Th}/^{208}\text{Pb}$ age of 319 ± 10 Ma, table 3) and was not considered for the calculation of the concordia
640 age. The 296 Ma age is consistent within errors with the age obtained on the high Th/U monazite of
641 sample 10Ag04 (300 ± 2 Ma) and can either be interpreted as the age of fluid percolation during the
642 mylonitic deformation or fluid exsolution from crystalizing melt of migmatites. Although monazite
643 m3 has the same compositional features as the other grains, it shows a spread of concordant dates in
644 the $^{232}\text{Th}/^{208}\text{Pb}$ vs $^{238}\text{U}/^{206}\text{Pb}$ concordia diagram. This spread in age along the concordia has been
645 observed in all analyzed samples, especially 10Ag02 and 11Ag03 (Figure 11a and c), it could
646 reflect a younger partial lead loss. We speculate that this isotopic disturbance could be the result of
647 localized fluid percolation during a Cretaceous event (ca. 100Ma) that affects the Pyrenees range
648 (Vitrac-Michard & Allègre, 1975, Boulvais et al., 2007, Poujol et al., 2010).

649

650

651 **6 DISCUSSION**

652

653

654 Our new geochronological data combined with phase relation modeling suggest that peak
655 metamorphism in the gneissic core was achieved at *c.* 305 Ma and that the massif was affected by
656 deformation between 300 Ma and 296 Ma. The age of metamorphism in the upper Paleozoic
657 sequence was not directly and quantitatively constrained by geochronology but we assume it is
658 related to the same late Variscan event. In the following, we will see that the finite metamorphic
659 field gradient observed in the Agly massif results from the superposition of a thermal (magmatic
660 and metamorphic) event (305 Ma) and a later tectonic (296-300 Ma) event.

661 **6.1 Geothermal gradient during the main metamorphic event (*c.* 305 Ma)**

662 Figure 12 shows the reconstructed metamorphic gradient for the entire rock column of the Agly
663 massif. It can be clearly seen that the geothermal gradient of the Agly massif is not linear and does
664 not result from a purely conductive heat transfer. The middle crust preserved in the gneissic core of
665 the Agly massif shows a very low to near isothermal gradient ($\sim < 8^{\circ}\text{C}/\text{km}$), while the low pressure
666 assemblages in the upper crust (i.e. andalusite-sillimanite transition, cordierite stable) defines a
667 significantly higher geothermal gradient ($> 50^{\circ}\text{C}/\text{km}$) in the Late Cambrian – Early Ordovician
668 sequence. This thermal structure of the continental crust has been previously described in high-
669 temperature and mid-crustal granulite terranes (Hollister, 1982; Patiño-Douce et al. 1990; De Yoreo
670 et al. 1991; Thompson & England, 1984; Thompson, 1999). Two different tectonic settings have
671 been called upon to explain such abnormal geothermal gradients. First, rifting resulting in an
672 extremely thin continental crust, with a possible mantle derived basaltic sill intrusion in the lower
673 crust providing sufficient heat to reach such high temperatures. This has been proposed in the
674 Pyrenean belt by Wickham and Oxburgh (1985; 1987), partly based on stable isotopes signature in
675 the uppermost crust (equivalent of the Late Cambrian - Early Ordovician sequence in the Agly
676 massif). The second alternative model is referred as the “melt-enhanced geotherm” (Depine et al.
677 2008) for which the combined effect of (1) upward heat advection associated with melt transfer and
678 (2) thermal buffering in the middle crust due to dehydration-melting reactions (either biotite or
679 hornblende breakdown reaction). In the case of the Agly massif several arguments are in favor of a
680 melt-enhanced thermal structure at *c.* 305 Ma:

681

682 *1) Contemporaneous magmatism and metamorphism at ca. 305 Ma.*

683 The main metamorphic event responsible for the abnormal geothermal gradient at 305 Ma is coeval

684 with a widespread magmatic event between 308 and 304 Ma (Figures 13a and b). In the deepest part
685 of the Agly crustal section, the Ansignan charnockite and the Cassagnes sills were emplaced at 307
686 ± 3 Ma and 308 ± 3 Ma, as a 500 to 800 m laccolith and decameter sills, respectively, parallel with
687 the main gently dipping foliation developed at peak metamorphic conditions. The upper part of the
688 gneissic core and the micaschist belonging to the Paleozoic sequence are intruded by the kilometer
689 thick Tournefort diorite at 308 ± 1 Ma and St Arnac granite at 304 ± 5 Ma that is exposed on a 25
690 km^2 surface (Olivier et al., 2008).

691

692 2) *Melt source and upward advection of heat by melt*

693 The Ansignan charnockite is a composite laccolith intrusive that consists of a massive ~ 500 to 800
694 m sill of orthopyroxene \pm garnet and K-feldspar megacrysts granite (i.e. the charnockite) associated
695 with norite bodies up to 300 m in its core and garnet-bearing leucocratic granites in its upper
696 margins. The source of the charnockite and associated magmatic rocks has been a matter of debate
697 in the 1980's (Fonteilles, 1981; Fourcade, 1981; Pin, 1989). All these studies agreed that the
698 charnockite was related to the partial melting of continental crust and more particularly
699 metasediments. Pin (1989) who conducted the most extensive isotopic analysis on the different
700 lithologies, suggested that the charnockitic magma without garnet (the more widespread facies of
701 the charnockitic complex), characterized by $\epsilon\text{Nd}_{300\text{Ma}}$, ranging from -6.4 and -4.4 and $^{87}\text{Sr}/^{86}\text{Sr}_i =$
702 0.7079 was produced by partial melting of metasediments due to the intrusion of contaminated
703 mafic magmas, corresponding to the norite bodies ($\epsilon\text{Nd}_{300\text{Ma}} = -2.5$ to -3.4 and $^{87}\text{Sr}/^{86}\text{Sr}_i = 0.7062-$
704 0.7067). These charnockitic magmas are characterized by a strong HREE fractionation (Fourcade,
705 1981; Tournaire-Guille et al., 2019, Figure 11b) suggesting that melts, produced by a high degree of
706 partial melting, were in equilibrium with a garnet-rich restite at a pressure greater than 6 kbar (see
707 below and Figure 13a). Chemical exchange between the mantle-derived mafic magmas with lower
708 crust-derived magmas resulted in a moderate Nd and Sr isotopic hybridization. Pin (1989) invoked
709 a second stage corresponding to the ascent and emplacement of this hybridized magma (norite and
710 charnockite) into upper crustal levels, corresponding to the present day gneissic core of the Agly
711 massif, at conditions estimated at 0.5 ± 0.05 GPa (~18 to 22 km) at $750 \pm 100^\circ\text{C}$ (Vielzeuf, 1984;
712 1986 and Figures 13a and b). The latent heat of crystallizing magmas induced partial melting of the
713 surrounding metasedimentary host-rock and the formation of the garnet-bearing charnockite and
714 leucogranites commonly observed at the margins of the intrusions. These garnet-bearing magmas
715 are characterized by a stronger crustal signature with the lowest $\epsilon\text{Nd}_{300\text{Ma}} = -6.4$ and -7.3 and the
716 highest- $^{87}\text{Sr}/^{86}\text{Sr}_i = 0.7109 - 0.7127$ recorded in the Ansignan intrusive complex.

717 The Cassagnes granodiorite, that consists of K-feldspar-bearing megacrystic sills of about 10 meters
718 thick, has a close age at 308 ± 3 Ma and very similar major / trace element composition to the

719 Ansignan charnockite (see Figures 10 and 11 in Tournaire-Guille et al., 2019). Therefore, we
720 suggest that both magmas have the same origin and source depth. The main difference between
721 them is that Cassagnes sills do not contain orthopyroxene nor garnet probably because they were
722 emplaced in a much shallower crustal level than the Ansignan granodiorite. Based on P-T
723 constrains on kinzigite located near the Cassagnes sills (10Ag06 and 11Ag03) on the eastern part of
724 the gneissic core, we suggest that they were emplaced at 0.5 GPa at 740°C corresponding to a depth
725 of ~ 18 km (Figures 13a and b).

726

727 The Tournefort diorite and Saint-Arnac granite are calc-alkaline magmas, similar to the other major
728 late-Variscan intrusions in the Pyrenees like the granite of Millas, Quérigut, Saint Laurent,
729 Maladetta or Mont-Louis. They are interpreted as the result of the emplacement of magmas in the
730 upper crust issued from partial melting of a deep old magmatic continental crust or hybridization of
731 deep seated crustal magmas with mantle-derived basalt intrusive and related to continental strike
732 slip and exhumation tectonics during the late Variscan collision (Lagarde et al., 1992).

733 It is clear from field observations that the Saint-Arnac granite and Tournefort diorite were not
734 produced in-situ but rather transferred from an unknown depth in the deep crust to the upper
735 Paleozoic sequence. Because the Tournefort diorite intruded andalusite-bearing micaschist, we
736 estimate the maximum depth of emplacement at about 11 km based on the 0.3 GPa pressure
737 estimated on the host rock (Figures 12 and 13a). Field evidence, like surrounding rocks xenoliths,
738 magma mingling and diorite enclaves in the granite, suggests that the Saint Arnac pluton is located
739 at the same depth in the micaschist. The granite intruded all the Ordovician micaschist and schist
740 series up to the Devonian marbles found as decameter xenolith in the wall of the granite. We
741 therefore suggest that the Saint Arnac granite has a minimum thickness of ~2500 m, corresponding
742 to the estimated thickness of the Ordovician series. The Saint-Arnac granite would have been
743 emplaced in the depth bracket of 9.5 and 12 km (Figure 13a). This estimation differs significantly
744 with Olivier et al. (2008), who suggested that the granite is 5 km thick with a roof located at a
745 shallow depth of 2.7 to 4 km (0.1 to 0.15 GPa). The emplacement of both intrusions is associated
746 with a local contact metamorphism that is characterized by partial melting around the diorite and
747 crystallization of large muscovite flakes in the surrounding micaschists around the granite and
748 micaschist xenoliths.

749 At the scale of the Agly massif, all these magmatic intrusions represent a significant volume that is
750 difficult to establish with confidence but may be greater than 30% of the basement (Figure 1). Their
751 migration from a deep source, currently not accessible in the exposed Agly massif, towards upper
752 crustal levels constitutes a very efficient and dynamic heat advection process. The crystallization of
753 late muscovite in micaschists around the Saint-Arnac granite and partial melting surrounding the

754 Tournefort diorite are consistent with magmatic heat advection in the previously LT Paleozoic
755 sequence. In the gneissic core, the upward heat advection during melt transfer and heat released
756 during the crystallization of magmas would increase temperature. This is in good agreement with
757 the observation of high temperatures ranging from 730 °C to 790 °C for pressure from 0.49 to 0.65
758 GPa (Figure 13b) for the entire gneissic core. At these depths, with a steady state-geotherm, the
759 temperatures would only be about 400-600 °C (figure 13a). The juxtaposition of high-grade rocks
760 from the lower crust as the explanation of the metamorphic gradient observed in the Agly is thus a
761 very unlikely explanation. These high temperatures cannot be achieved without the additional heat
762 source from magmas, even with a high mantle heat flux (Figure 13a). We suggest that the low
763 gradient at about 750 °C in the gneissic core is the combination of melt migration, plutons
764 formation and thermal buffering by the biotite-dehydration melting reaction that produced garnet
765 +/- cordierite. In contrast, the geothermal gradient in the upper crust, above the shallower intrusion
766 to the surface, is significantly higher (~ 55 °C/km) and correspond to a diffusive geothermal
767 gradient (compare Figures 13a and b). The orthogneisses of the gneissic core might not have been
768 as affected as the metapelites by the thermal buffering since they are less fertile in terms of melt
769 production (Schorn, Diener, Powell, & Stüwe, 2018). Nevertheless, they represent only a marginal
770 portion of the gneissic core (Figure 1). Thus, the temperatures computed from metapelites, buffered
771 by the biotite dehydration-melting reaction, can be interpreted as representative of the thermal state
772 of the gneissic core.

773

774 **6.2 Thinning of the massif**

775 Evidences for a major thinning of the Agly massif have been well accepted for decades now,
776 especially based on the difference between depth inferred from previous geothermobarometric
777 studies and thickness of the rock column of the massif in its present geometry. This thickness has
778 been inferred with paleo-pressure calibrations to be of about 11 km between the top of the Paleozoic
779 Jujol group and the bottom of the Charnockite and represents now a lithologic pile of only 5-6 km
780 of exposed rocks. Nevertheless, the timing and importance of this thinning is still a matter of
781 debate, as recently outlined by the succession of publications (Olivier et al. 2004; 2008; Olivier
782 2013; Vauchez et al. 2013a; 2013b). Even more recently, two studies have rejuvenated this debate
783 with new data, using (U-Th)/He (Ternois et al., 2019) and U-Pb (Odlum & Stockli, 2019) in both
784 zircons and apatite. The first study founded that the Agly massif never experienced temperature
785 higher than 250 °C during Cretaceous rifting while the second study argued that the gneissic core
786 was still at temperatures higher than 450 °C before rifting. In terms of the thinning itself and
787 concerning the late Variscan tectonics only, two different deformation settings have been proposed.

788 First, the presence of one major subtracting zone responsible for the main thinning of the massif
789 was proposed by Bouhaillier et al. (1991) and Delay (1990). This detachment zone would act as a
790 major normal fault located at the boundary between the Late Cambrian – Early Ordovician
791 sequence (Jujol group) and the gneissic core. It has been referred to the Latour-Caladroy mylonitic
792 zone (Figure 1 and labelled “Caladroy SZ” on the cross-section, figure 2) since many mylonites
793 with normal shear behavior have been observed between the city of Latour-de-France and the castle
794 of Caladroy. In contrast, Olivier et al. (2008) argued that the thinning of the massif was
795 accommodated by numerous normal shear zones over the entire massif.

796 The reconstruction of the geothermal gradient in the Jujol group and in the gneissic core from the
797 present study clearly shows a pressure gap of 0.15 GPa between the bottom of the Late Cambrian –
798 Early Ordovician sequence and the uppermost level of kinzigite (Figure 12). A simple pressure
799 conversion into depth (using an average density of 2.7), indicates that about 5.5 km of rocks may
800 have been subtracted by the Latour-Caladroy mylonites (Figure 12c). The fact that most of the
801 deformation and subtraction was localized at the boundary between the partially molten micaschists
802 and the gneissic core is not surprising since partial melting induces a major strength drop when melt
803 proportion reaches 7 vol% (Rosenberg & Handy, 2005). The onset of partial melting triggered by
804 muscovite dehydration reaction is known to produce under 10% of melt (White, Powell, & Holland,
805 2001), such value would then be in good agreement with deformation experiments.

806 We also suggest that thinning and associated rock subtraction is not restricted to the Latour-
807 Caladroy mylonite but also occur within the gneissic core. Pressures estimated for the deepest
808 kinzigite level close to the Charnockite are 0.62-0.66 GPa (10Ag01 and 10Ag02, Figure 12). This
809 would give a pressure difference between the shallowest and the deepest kinzigite levels for the
810 gneissic core of about 0.10 to 0.15 GPa, or a thickness of about 3.7 to 5.5 km. Since the present-day
811 gneissic core thickness do not exceed 2.5-3 km, we suggest that the numerous mylonites observed
812 throughout the entire gneissic core might be responsible for the remaining thinning of the massif (as
813 quoted Ansignan and gneissic core mylonites on Figure 12c).

814 Monazite overgrowths with highly variable Th/U ratio from mylonitized kinzigites yield ages of
815 about 296-300 Ma (samples 11Ag03 and 11Ag04; Figures 11c and 11d). These overgrowths may
816 have been produced by fluid-assisted dissolution/ precipitation during localized fluid percolation in
817 shear zones pathways. Furthermore, the highly variable Th/U ratio is also a good evidence that
818 monazite rims were not in equilibrium rock-wide but rather locally equilibrated with a fluid. The
819 origin of the fluid responsible for the dissolution/precipitation of the overgrowth could be the result
820 of crystalizing melt from migmatites. This would require to be near the solidus at significantly
821 lower temperature and pressure than 0.6 GPa and 750-790 °C determined at 305 Ma. Such drop in
822 pressure and temperature would likely be the result of tectonic assisted exhumation, such that the

823 age at 296-300 Ma would be the age of the thinning of the massif. To conclude, we suggest that the
824 thinning of the Agly massif occurred between 300 and 296 Ma after peak metamorphism and the
825 main magmatic event at *c.* 305 Ma. The Cretaceous thinning during rifting prior to the Pyrenean
826 orogen would not have significantly disturbed the geometry acquired at the end of the Variscan
827 orogeny, in agreement with the (U-Pb)/He on zircons and apatite data from Ternois et al. (2019).
828 Nevertheless, blocs might have slightly moved along the E-W Pyrenean fault that crosscut the
829 massif, especially the southernmost bloc where the Ansignan charnockite is located, that most
830 probably moved to slightly upper levels along the E-W fault located in the Caramany lake.

831

832

833 **7 CONCLUSION**

834

835 The detailed petrological and geothermobarometric data from the present study shows that
836 the Agly massif has experienced an abnormal thermal state during late-Variscan orogeny. This has
837 resulted in a very high geothermal gradient of 55 °C/km in the upper crust (above 13 km depth) and
838 a near isothermal gradient in the middle crust. New monazite U-Th-Pb geochronology show that
839 this metamorphic event took place at *c.* 305 Ma. This abnormal geothermal gradient is the
840 consequence of the coeval emplacement of several intrusions at different structural level during a
841 limited time period *c.* 304-308 Ma. The heat provided by these intrusions allowed the middle crust
842 to reach partial melting temperatures at depth below 13 km, and very high temperatures, i.e.
843 ~750°C, between 18 and 25 km depth and be responsible of a “regional contact metamorphism”.
844 The biotite dehydration-melting reaction, strongly endothermic, buffered temperature in the middle
845 crust, resulting in the observed near isothermal geothermal gradient. The high geothermal gradient
846 in the upper crust is mostly due to heat conduction between the anomalously hot middle crust and
847 the cold surface.

848 This gradient was latter disturbed by normal mylonitic shear zones, resulting in the thinning
849 of the massif from a thickness of 15 km to a final 5-6 km thickness. Most of this thinning was
850 concentrated within a major detachment zone located at the onset of partial melting, between the
851 Late Cambrian – Early Ordovician sequence and the gneissic core. This detachment zone was
852 responsible for the subtraction of 5-6 km of rocks thickness. The remaining thinning most likely
853 took place at several levels inside the gneissic core, resulting in the abundance of small mylonitic
854 zones. The tectonic juxtaposition of a very hot middle crust (i.e. ~750 °C) and a colder upper crust
855 probably increased the temperature of the later. Nevertheless, due to the already existing thermal
856 structure resulting of the metamorphic event at *c.* 305 Ma, temperatures in the upper crust were
857 already higher than normal, close to 660 °C at the contact with the gneissic core. The temperature

858 increase due to thinning was only marginal and well below the precision of any present
859 geothermobarometric method. This thinning event could be linked to the second age observed in
860 monazite overgrowths and determined to be at c. 296-300 Ma. Nevertheless, this should be the
861 focus of a detailed geochronologic study, aiming specific deformed monazites inside strongly
862 deformed samples to directly date the thinning event.

863

864

865 REFERENCES

866 Andrieux, P., (1982). Conditions de cristallisation et évolution paragenétique d'une charnockite
867 hercynienne: le complexe granulitique d'Ansignan (massif de l'Agly, Pyrénées orientales):
868 *Bulletin Minéralogique*, 105, 253–266.

869 Autran, A., Fonteilles, M., & Guitard, G. (1966) Discordance du Paléozoïque inférieur
870 métamorphique sur un socle gneissique antéhercynien dans le massif des Albères (Pyrénées
871 orientales). *C. R. Acad. Sc. Paris, série D*, 263, 317–320.

872 Autran, A., Fonteilles, M., & Guitard, G. (1970). Relations entre intrusions de granitoides,
873 l'anatexie et le métamorphisme régional considérées principalement du point de vue du rôle de
874 l'eau : Cas de la chaîne hercynienne des Pyrénées Orientales. *Bulletin de la Société géologique*
875 *de France*, 12(4), 673–731.

876 Berman, R. G. (1988). Internally-Consistent Thermodynamic Data for Minerals in the System
877 Na₂O-K₂O-CAO-MgO-FeO-Fe₂O₃-AL₂O₃-SiO₂-TiO₂-H₂O-CO₂. *Journal of Petrology*, 29,
878 445–522.

879 Bouhallier, H., Choukroune, P., & Ballèvre, M. (1991). Evolution structurale de la croûte profonde
880 Hercynienne: exemple du massif de l'Agly (Pyrénées Orientales, France). *Comptes Rendus De*
881 *l'Académie Des Sciences, Paris*, 312, 647–654.

882 Brown, M. (2007). Metamorphic Conditions in Orogenic Belts: A Record of Secular Change. *Inter-*
883 *national Geology Review*, 49, 193–234.

884 Brown, M., & Kothonen, F. J. (2009). Some Remarks on Melting and Extreme Metamorphism of
885 Crustal Rocks. In *Physics and Chemistry of the Earth's Interior* (pp. 67–87). New York, NY:
886 Springer New York.

887 Carreras, J., & Capella, I. (1994). Tectonic levels in the Palaeozoic basement of the Pyrenees: a
888 review and a new interpretation. *Structures and Tectonics at Different Lithospheric Levels*,
889 16(11), 1509–1524.

- 890 Casas, J.M., & Palacios, T. (2012). First biostratigraphical constraints on the pre-Upper Ordovician
891 sequences of the Pyrenees based on organic-walled microfossils. *Comptes Rendus Geoscience*,
892 344, 50–56.
- 893 Choukroune, P. (1992). Tectonic evolution of the Pyrenees. *Annual Review of Earth and Planetary*
894 *Sciences*, 20, 143–158.
- 895 Clerc, C., & Lagabriele, Y. (2014). Thermal control on the modes of crustal thinning leading to
896 mantle exhumation: Insights from the Cretaceous Pyrenean hot paleomargins. *Tectonics*, 1340–
897 1359.
- 898 Cochelin, B., Lemirre, B., Denèle, Y., de Saint-Blanquat, M., Lahfid, A., & Duchêne, S. (2018)
899 Structural inheritance in the Central Pyrenees: the Variscan to Alpine tectonometamorphic evo-
900 lution of the Axial Zone. *Journal of the Geological Society*, 175, 336–351.
- 901 Cocherie, A., Baudin, T., Autran, A., Guerrot, C., Fanning, C. M., & Laumonier, B. (2005). U-Pb
902 zircon (ID-TIMS and SHRIMP) evidence for the early ordovician intrusion of metagranites in
903 the late Proterozoic Canaveilles Group of the Pyrenees and the Montagne Noire (France). *Bul-*
904 *letin de la Société géologique de France*, 176, 269–282.
- 905 Connolly, J. A. D., & Petrini, K. (2002). An automated strategy for calculation of phase diagram
906 sections and retrieval of rock properties as a function of physical conditions. *Journal of Meta-*
907 *morphic Geology*, 1–12.
- 908 de Capitani, C., & Petrakakis, K. (2010). The computation of equilibrium assemblage diagrams
909 with Theriak/Domino software. *American Mineralogist*, 95, 1006–1016.
- 910 Delay, F. (1990). Etude structurale du massif de l'Agly (Pyrénées orientales). *Mémoire de la*
911 *Société Géologique du Nord, Lille*, 17, 393p.
- 912 Denèle, Y., Olivier, P., Gleizes, G., & Barbey, P. (2007). The Hospitalet gneiss dome (Pyrenees)
913 revisited: lateral flow during Variscan transpression in the middle crust. *Terra Nova*, 19(6),
914 445–453.
- 915 Denèle, Y., Olivier, P., Gleizes, G., & Barbey, P. (2009). Decoupling between the middle and upper
916 crust during transpression-related lateral flow: Variscan evolution of the Aston gneiss dome
917 (Pyrenees, France). *Tectonophysics*, 477(3-4), 244–261.
- 918 De Yoreo, J. J., Lux, D. R., Guidotti, C. V., Decker, E. R., & Osberg, P. H. (1989). The Acadian
919 thermal history of western Maine. *Journal of Metamorphic Geology*, 7, 169–190.
- 920 Fonteilles, M., & Guitard, G. (1964). L'effet de socle dans le métamorphisme Hercynien de
921 l'enveloppe Paléozoïque des gneiss des Pyrénées. *Comptes Rendus Hebdomadaires des*

- 922 *séances de l'Académie des Sciences*, 258, 4299–4302.
- 923 Fonteilles, M. (1976). Essai d'interprétation des compositions chimiques des roches d'origines
924 métamorphique et magmatique du massif hercynien de l'Agly. *Université de Paris*, 684p.
- 925 Gasquet, D., Bertrand, J.M., Paquette, J.L., Lehmann, J., Ratzov, G., De Ascensão Guedes R.,
926 Tiepolo, M., Boullier, A.M., Scaillet, S. & Nomade, S. (2010). Miocene to Messinian
927 deformation and hydrothermalism in the Lauzière Massif (French Western Alps): New U-Th-
928 Pb and Argon ages. *Bull. Soc. Géol. France*, 181(3), 227-241.
- 929 Gibson, R. L. (1991). Hercynian low-pressure-high-temperature regional metamorphism and sub-
930 horizontal foliation development in the Canigou massif, Pyrenees, France—Evidence for
931 crustal extension. *Geology*, 19(4), 380–383.
- 932 Gonçalves, G.O., Lana, C., Scholz, R., Buick, I.S., Gerdes, A., Kamo, S.L., Corfu, F., Marinho,
933 M.M., Chaves, A.O., Valeriano, C., & Nalini Jr, H.A., (2016). An assessment of monazite
934 from the Itambé pegmatite district for use as U-Pb isotope reference material for
935 microanalysis and implications for the origin of the "Moacyr" monazite. *Chemical Geology*,
936 424, 30-50.
- 937 Groppo, C., Rolfo, F., & Indares, A. (2012) Partial Melting in the Higher Himalayan Crystallines of
938 Eastern Nepal: the Effect of Decompression and Implications for the “Channel Flow” Model.
939 *Journal of Petrology*, 53, 1057–1088.
- 940 Guitard, G., Vielzeuf, D., & Martinez, F. (1996) Le Métamorphisme Hercynien. In A. Barnolas and
941 J.C. Chiron, Eds., Synthèse Géologique et Géophysique des Pyrénées - Tome 1 - Cycle Hercy-
942 nien pp. 501–584.
- 943 Holland, T.J.B., and Powell, R. (1998) An internally consistent thermodynamic data set for phases
944 of petrological interest. *Journal of Metamorphic Geology*, 16, 309–343.
- 945 Holland, T. J. B., & Powell, R. (2011). An improved and extended internally consistent thermody-
946 namic dataset for phases of petrological interest, involving a new equation of state for solids.
947 *Journal of Metamorphic Geology*, 29, 333–383.
- 948 Hollister, L. S. (1982). Metamorphic evidence for rapid (2 mm/yr) uplift of a portion of the central
949 gneiss complex, coast mountains, B.C. *The Canadian Mineralogist*, 20, 319–332.
- 950 Hurai, V., Paquette, J.-L., Huraiová, M., & Konečný, P. (2010). Age of deep crustal magmatic
951 chambers in the intra-Carpathian back-arc basin inferred from LA-ICPMS U-Th-Pb dating of
952 zircon and monazite from igneous xenoliths in alkali basalts. *Journal of Volcanological and*
953 *Geothermal Research*, 198, 275-287.
- 954 Jackson, S.E., Pearson, N.J., Griffin, W.L., & Belousova, E.A. (2004). The application of laser

- 955 ablation-inductively coupled plasma-mass spectrometry to in situ U–Pb zircon geochronology.
956 *Chemical Geology*, 211, 47–69.
- 957 Kim, J., & Cho, M. (2003). Low-pressure metamorphism and leucogranite magmatism, northeastern
958 Yeongnam Massif, Korea: implication for Paleoproterozoic crustal evolution. *Precambrian Re-*
959 *search*, 122, 235–251.
- 960 Lagarde J.L., Capdevila R., & Fourcade S. (1992). Granites et collision continentale : exemple des
961 grantoïdes carbonifères dans la chaîne hercynienne ouest-européenne. *Bull. Soc. Géol. France*,
962 163/5, 597–610.
- 963 Laumonier, B. (1998). Les Pyrénées centrales et orientales au début du Paléozoïque (Cambrien s.l.):
964 évolution paléogéographique et géodynamique. *Geodinamica Acta*, 11, 1–11.
- 965 Ludwig, K.R. (2001). User’s manual for Isoplot/Ex Version 2.49, a geochronological toolkit for
966 Microsoft Excel. Berkeley Geochronological Center, Special Publication 1a, Berkeley, USA,
967 55 pp.
- 968 Lux, D. R., DeYoreo, J. J., Guidotti, C. V., & Decker, E. R. (1986). Role of plutonism in low-
969 pressure metamorphic belt formation. *Nature*, 323, 794–797.
- 970 Odlum, M.L., and Stockli, D.F. (2019) Thermotectonic evolution of the North Pyrenean Agly Mas-
971 sif during Early Cretaceous hyperextension using multi- mineral U- Pb thermochronometry.
972 *Tectonics*, 2018TC005298–54.
- 973 Okay, A.I., Sunal, G., Tüysüz, O., Sherlock, S., Keskin, M., & Kylander-Clark, A.R.C. (2013)
974 Low-pressure-high-temperature metamorphism during extension in a Jurassic magmatic arc,
975 Central Pontides, Turkey. *Journal of Metamorphic Geology*, 32, 49–69.
- 976 Olivier, P., Gleizes, G., & Paquette, J. L. (2004). Gneiss domes and granite emplacement in an
977 obliquely convergent regime: New interpretation of the Variscan Agly Massif (Eastern
978 Pyrenees, France). *Geological Society of America, Special Paper*, 380, 229–242.
- 979 Olivier, P., Gleizes, G., Paquette, J.-L., & Muñoz Saez, C. (2008). Structure and U–Pb dating of the
980 Saint-Arnac pluton and the Ansignan charnockite (Agly Massif): a cross-section from the upper
981 to the middle crust of the Variscan Eastern Pyrenees. *Journal of the Geological Society*, 165,
982 141–152.
- 983 Olivier, P. (2013). Comment on “Preorogenic exhumation of the North Pyrenean Agly massif
984 (Eastern Pyrenees-France)” by A. Vauchez et al. *Tectonics*, 34, 2275–2278.
- 985 Pattison, D.R.M., & Tracy, R.J. (1991) Phase equilibria and thermobarometry of metapelites. *Re-*
986 *views in Mineralogy and Geochemistry*, 26, 105–206.

- 987 Pattison, D. R. M., Spear, F. S., Debuhr, C. L., Cheney, J. T., and Guidotti, C. V. (2002). Thermo-
988 dynamic modelling of the reaction muscovite+cordierite->Al₂SiO₅+biotite+quartz+H₂O: con-
989 straints from natural assemblages and implications for the metapelitic petrogenetic grid. *Jour-*
990 *nal of Metamorphic Geology*, 20, 99–118.
- 991 Pattison, D. R. M., and Vogl, J. J. (2005). Contrasting sequences of metapelitic mineral-
992 assemblages in the aureole of the tilted Nelson natholith, British Columbia: Implications for
993 phase equilibria and pressure determination in andalusite-silimanite-type settings. *The Cana-*
994 *dian Mineralogist*, 43, 51–88.
- 995 Pattison, D. R. M., & Tinkham, D. K. (2009). Interplay between equilibrium and kinetics in pro-
996 grade metamorphism of pelites: an example from the Nelson aureole, British Columbia. *Jour-*
997 *nal of Metamorphic Geology*, 27, 249–279.
- 998 Pattison, D. R. M., de Capitani, C., & Gaidies, F. (2011). Petrological consequences of variations in
999 metamorphic reaction affinity. *Journal of Metamorphic Geology*, 29, 953–977.
- 1000 Pattison, D. R. M., & Debuhr, C. L. (2015). Petrology of metapelites in the Bugaboo aureole, Brit-
1001 ish Columbia, Canada. *Journal of Metamorphic Geology*, 33, 437–462.
- 1002 Paquet, J., & Mansy, J.-L. (1991). La structure de l'Est des Pyrénées (transversale du massif de
1003 l'Agly) : un exemple d'amincissement crustal. *Comptes Rendus De l'Académie Des Sciences*,
1004 *Paris*, 312, 913–919.
- 1005 Paquette, J.L., & Tiepolo, M. (2007). High resolution (5 µm) U-Th-Pb isotopes dating of monazite
1006 with excimer laser ablation (ELA)-ICPMS. *Chemical Geology*, 240, 222-237.
- 1007 Paquette, J.L., Piro, J.L., Devidal, J.L., Bosse, V., & Didier, A. (2014). Sensitivity enhancement in
1008 LA-ICP-MS by N₂ addition to carrier gas: application to radiometric dating of U-Th-bearing
1009 minerals. *Agilent ICP-MS Journal*, 58, 4-5.
- 1010 Poujol, M., Boulvais, P., & Košler, J. (2010). Regional-scale Cretaceous albitization in the Pyre-
1011 nees: evidence from in situ U–Th–Pb dating of monazite, titanite and zircon. *Journal of the*
1012 *Geological Society*, 167, 751–767.
- 1013 Powell, R., Guiraud, M., & White, R.W. (2005). Truth and beauty in metamorphic phase-equilibria:
1014 conjugate variables and phase diagrams. *The Canadian Mineralogist*, 43, 21–33.
- 1015 Riel, N., Mercier, J., & Weinberg, R. (2015) Convection in a partially molten metasedimentary
1016 crust? Insights from the El Oro complex (Ecuador). *Geology*, 44, 31–34.
- 1017 Schorn, S., Diener, J.F.A., Powell, R., & Stüwe, K. (2018) Thermal buffering in the orogenic crust.
1018 *Geology*, 46, 643–646.

- 1019 Spear, F.S., & Pyle, J.M. (2010). Theoretical modeling of monazite growth in a low-Ca metapelite.
1020 *Chemical Geology*, 273, 111–119.
- 1021 Respaut, J. P., & Lancelot, J. R. (1983). Datation de la mise en place synmétamorphe de la chan-
1022 rockite d'Ansignan (massif de l'Agly) par la méthode U/Pb sur zircons et monazites. *Neues*
1023 *Jahrbuch Mineralogie Abh*, 147, 21–34.
- 1024 Saint Blanquat, M., Lardeaux, J. M., & Brunel, M. (1990). Petrological arguments for high-
1025 temperature extensional deformation in the Pyrenean Variscan crust (Saint Barthélémy Massif,
1026 Ariège, France). *Tectonophysics*, 177(1), 245–262.
- 1027 Saint-Blanquat, M. (1993). La faille normale ductile du massif du Saint Barthélémy. Evolution her-
1028 cynienne des massifs nord-pyrénéens catazonaux considérée du point de vue de leur histoire
1029 thermique. *Geodinamica Acta*, 6(1), 59–77.
- 1030 Soula, J. C., Debat, P., Deramond, J., Guchereau, J. Y., Lamouroux, C., Pouget, P., & Roux, L.
1031 (1986). Structural evolution of the Hercynian central Pyrenees. *Bulletin de la Société Géolo-*
1032 *gique de France*, 2, 79–93.
- 1033 Spear, F. S., & Cheney, J. T. (1989). A petrogenetic grid for pelitic schists in the system SiO₂-
1034 Al₂O₃-FeO-MgO-K₂O-H₂O. *Contributions to Mineralogy and Petrology*, 101, 149–164.
- 1035 Ternois, S., Odlum, M., Ford, M., Pik, R., Stockli, D., Tibari, B., Vacherat, A., and Bernard, V.
1036 (2019) Thermochronological Evidence of Early Orogenesis, Eastern Pyrenees, France. *Tecton-*
1037 *ics*, 38, 1308–1336.
- 1038 Thompson, A. B., & England, P. C. (1984). Pressure-Temperature-Time Paths of Regional Meta-
1039 morphism II. Their Inference and Interpretation using Mineral Assemblages in Metamorphic
1040 Rocks. *Journal of Petrology*, 25, 929–955.
- 1041 Tomascak, P.B., Krogstad, E.J., & Walker, R.J. (1996). U-Pb monazite geochronology of granitic
1042 rocks from Maine: implications for late Paleozoic tectonics in the northern Appalachians.
1043 *Journal of Geology*, 104, 185-195.
- 1044 Tournaire Guille, B., Olivier, P., Paquette, J.-L., Bosse, V., and Guillaume, D. (2018) Evolution of
1045 the middle crust of the Pyrenees during the Paleozoic: new data on the plutonic rocks from the
1046 North Pyrenean Agly Massif. *International Journal of Earth Sciences*.
- 1047 Trap, P., Roger, F., Cenki-Tok, B., & Paquette, J.-L. (2016) Timing and duration of partial melting
1048 and magmatism in the Variscan Montagne Noire gneiss dome (French Massif Central). *Interna-*
1049 *tional Journal of Earth Sciences*, 106, 453–476.
- 1050 Van Achterbergh, E., Ryan, C.G., Jackson, S.E., & Griffin, W.L. (2001). Data reduction software

- 1051 for LA-ICP-MS. In *Laser ablation-ICPMS in the earth science*. P. Sylvester ed. *Mineralogical*
1052 *Association of Canada*, 29, 239-243.
- 1053 Van den Eeckhout, B., & Zwart, H. J. (1988). Hercynian crustal-scale extensional shear zone in the
1054 Pyrenees. *Geology*, 16(2), 135–138.
- 1055 Vauchez, A., Clerc, C., Bestani, L., Lagabrielle, Y., Chauvet, A., Lahfid, A., & Mainprice, D.
1056 (2013). Preorogenic exhumation of the North Pyrenean Agly massif (Eastern Pyrenees-France).
1057 *Tectonics*, 32, 95–106.
- 1058 Vauchez, A., Chauvet, A., Lagabrielle, Y., Mainprice, D., Bestani, L., Clerc, C., & Lahfid, A.
1059 (2013). Reply to comment by P. Olivier on “Preorogenic exhumation of the North Pyrenean
1060 Agly Massif (Eastern Pyrenees, France).” *Tectonics*, 32, 823–826.
- 1061 Vielzeuf, D. (1984). Relation de phases dans le faciès granulitique et implications géodynamiques.
1062 L'exemple des granulites des pyrénées. Université de Clermont-Ferrand II, PhD Thesis, 359p.
- 1063 Vielzeuf, D. (1996). Les massifs nord-pyrénéens à soubassement granulitique, in Barnolas, A., and
1064 Chiron J.C., eds., *Synthèse géologique et géophysique des Pyrénées: Introduction,*
1065 *Géophysique, Cycle hercynien*, Ed. BRGM - ITGE, 1, 502–521.
- 1066 Vitrac-Michard, A., & Allègre, C.J. (1975). ^{238}U - ^{206}Pb , ^{235}U - ^{207}Pb , Systematics on Pyrenean Base-
1067 ment. *Contributions to Mineralogy and Petrology*, 51, 205–212.
- 1068 White, R.W., Powell, R., & Holland, T.J.B. (2001). Calculation of partial melting equilibria in the
1069 system Na_2O - CaO - K_2O - FeO - MgO - Al_2O_3 - SiO_2 - H_2O . *Journal of Metamorphic Geology*, 19,
1070 139–153.
- 1071 Wickham, S. M., & Oxburgh, E. R. (1985). Continental rifts as a setting for regional metamor-
1072 phism. *Nature*, 318(6044), 330–333.
- 1073 Wickham, S. M., Oxburgh, E. R., Reading, H. G., & Vissers, R. L. M. (1987). Low-Pressure Re-
1074 gional Metamorphism in the Pyrenees and its Implications for the Thermal Evolution of Rifted
1075 Continental Crust [and Discussion]. *Philosophical Transactions of the Royal Society a:*
1076 *Mathematical, Physical and Engineering Sciences*, 321(1557), 219–242.
- 1077 Wohlers, A., & Baumgartner, L.P. (2012) Melt infiltration into quartzite during partial melting in
1078 the Little Cottonwood Contact Aureole (UT, USA): implication for xenocryst formation. *Jour-*
1079 *nal of Metamorphic Geology*, 31, 301–312.
- 1080

1081 **APPENDIX**

1082 Chemical system, software and activity-composition relationship model used for the
 1083 thermodynamic modelling.

Figure	Chemical system	Software	Thermodynamic database	Solid Solution	a-X models abbreviation	Reference
Fig . 6a and 6b	NCKFM ASHT	Perple_X	Holland and Powell (2002)	K-feldspar Plagioclase Melt White Mica Garnet Chlorite Cordierite Biotite Staurotide	San Pl(h) melt(HP) Pheng(HP) Gt(WPPH) Chl(HP) hCrd Bio(HP) St(HP)	Waldbaum and Thompson (1968) Newton et al. (1980) White et al. (2001) Holland & Powell (1998) White et al. (2005) Holland & Powell (1998)
Fig . 6c	KFMAS H	Perple_X	Holland and Powell (2002)	K-feldspar Plagioclase Melt White Mica Garnet Chlorite Cordierite Biotite Orthopyroxene Staurotide	San Pl(h) melt(HP) Mica(CHA) Gt(WPPH) Chl(HP) hCrd Bio(HP) Opx(HP) St(HP)	Waldbaum and Thompson (1968) Newton et al. (1980) White et al. (2001) Coggon & Holland (2002) White al. (2005) Holland et al. (1998) ideal mixing Holland et al. (1998) Powell and Holland (1999)

						ideal mixing
Fig . 6d	KFMAS H	Domino/Theriak	SPac14	same as Fig 6c	Ideal site mixing	
Fig . 8a and 8b	NCKFM ASHT	Perple_X	Holland and Powell (2002)	K-feldspar Plagioclase Melt White Mica Garnet Chlorite Cordierite Biotite Staurotide	San Pl(h) melt(HP) Mica(CHA Gt(WPPH) Chl(HP) hCrd Bio(HP) St(HP)	Waldbaum and Thompson (1968) Newton et al. (1980) White et al. (2001) Coggon & Holland (2002) White al. (2005) Holland et al. (1998) ideal mixing Holland et al. (1998) Ideal mixing

1084

1085

1086 references

Coggon, R., & Holland, T. J. B. (2002). Mixing properties of phengitic micas and revised garnet-phengite thermobarometers. *Journal of Metamorphic Geology*, 20(7), 683-696. <https://doi.org/10.1046/j.1525-1314.2002.00395.x>

Holland, T. J. B., & Powell, R. (1998). An internally consistent thermodynamic data set for phases of petrological interest. *Journal of Metamorphic Geology*, 16(3), 309-343. <https://doi.org/10.1111/j.1525-1314.1998.00140.x>

Newton, R. C., Charlu, T. V., & Kleppa, O. J. (1980). Thermochemistry of the high structural state plagioclases. *Geochimica et Cosmochimica Acta*, 44(7), 933-941. [https://doi.org/10.1016/0016-7037\(80\)90283-5](https://doi.org/10.1016/0016-7037(80)90283-5)

Powell, R., & Holland, T. (1999). Relating formulations of the thermodynamics of mineral solid solutions; activity modeling of pyroxenes, amphiboles, and micas. *American Mineralogist*, 84(1-2), 1-14. <https://doi.org/10.2138/am-1999-1-201>

Waldbaum, D. R., & Thompson, J. B. (1968). Mixing Properties Of Sanidine Crystalline Solutions .2. Calculations Based On Volume Data. *American Mineralogist*, 2000-2017.

White, R. W., Pomroy, N. E., & Powell, R. (2005). An in situ metatexite–diatexite transition in upper amphibolite facies rocks from Broken Hill, Australia. *Journal of Metamorphic Geology*, 23(7), 579-602.

<https://doi.org/10.1111/j.1525-1314.2005.00597.x>

White, R. W., Powell, R., & Holland, T. J. B. (2001). Calculation of partial melting equilibria in the system Na₂O–CaO–K₂O–FeO–MgO–Al₂O₃–SiO₂–H₂O (NCKFMASH). *Journal of Metamorphic Geology*, 19(2), 139-153.

<https://doi.org/10.1046/j.0263-4929.2000.00303.x>

1087

1088

1089

1090

1091

1092

1093 **Figure captions:**

1094

1095 Figure 1: Geographic and geologic setting of the Agly massif; a) situation of the Agly massif in the
1096 Pyrenees in respect to all Variscan massifs, modified after Olivier et al. (2004); b) geological map
1097 of the massif produced during this study; the E-W cross section is discontinuous to take into
1098 account the displacement along the Planèzes fault, which was most likely active during very late
1099 Variscan stage.

1100

1101

1102 Figure 2: Schematic E-W cross-section located on figure 1. The different shear zones (SZ) have
1103 been highlighted in dark black.

1104

1105 Figure 3: Petrography of the Late Cambrian – Early Ordovician samples, with increasing
1106 metamorphic grade from left to right and top to bottom. a) Polarized photomicrograph of a
1107 greenschist facies sample with sedimentary bedding and main schistosity; S_{n-1} microlithon shows
1108 the transition between chlorite grade and biotite grade. b) Polarized photomicrograph for a typical
1109 biotite grade sample, with biotite (Bt) and muscovite (Ms) in the main schistosity. c) Polarized
1110 photomicrograph of a cordierite grade sample, with a slightly rotated large poikilitic cordierite (Crd)
1111 porphyroblast with biotite, quartz and oxides inclusions. Biotite is also present in the matrix, in the
1112 main schistosity, as well as muscovite. d) Polarized photomicrograph of a cordierite-andalusite
1113 grade sample, with large poikilitic andalusite (And) porphyroblasts with biotite, quartz and oxides
1114 in inclusions. Biotite and muscovite are mainly present in the matrix aligned in the main schistosity,

1115 interbedded with quartz (Qtz) and plagioclase (Pl). e) Polarized photomicrograph of a sillimanite
1116 grade sample, with typical fibrolite (Sil) patches, aligned in the main foliation. Muscovite (Ms2) is
1117 only present as secondary mineral, discordant to the main foliation. f) Polarized photomicrograph of
1118 a partially melted sample, with small aggregates of quartz (Qtz), alkali feldspar (Kfs) and
1119 plagioclase (Pl), representing the remaining melt pockets. Biotite (Bt) and sillimanite (Sil) are
1120 aligned in the main foliation.

1121

1122

1123 Figure 4: Petrography for three kinzigite samples from different structural levels of the gneissic
1124 core, 10Ag11 located slightly above the Ansignan charnockite; 10Ag04 represents the deepest level,
1125 below the charnockite; 10Ag03 is the shallowest level, near the Cuxous castle at about 500m from
1126 the contact with the Late Cambrian – Early Ordovician sequence. a) polarized photomicrograph for
1127 10Ag11, with large garnet porphyroblasts and prismatic sillimanite (Sil) and biotite (Bt) aligned in
1128 the main foliation. Note the fresh cordierite grain on the lower right corner of the microphotograph.
1129 b) Polarized photomicrograph for sample 10Ag04, showing fractured garnet, fresh cordierite and
1130 monazite (Mnz) grains used for the geochronological study. c) Polarized photomicrograph of the
1131 sample 11Ag03, showing highly deformed K-feldspars (Kfs), grain size reduction for prismatic
1132 sillimanite (Sil) and retrogressed cordierite (“Crd”). Note the grain size reduction in figure b) and c)
1133 in the shear bands.

1134

1135

1136 Figure 5: Thompson-like AFM diagram projected from muscovite end-member. Black dots
1137 represent the XRF-analyses for the different samples of the Late Cambrian – Early Ordovician
1138 sequence. White dot corresponds to sample 10Ag16 considered as a representative composition (see
1139 text for explanations).

1140

1141

1142

1143 Figure 6: Thermodynamic modelling for the Late Cambrian – Early Ordovician sequence. Sample
1144 10Ag16 was selected since it is representative of the composition for the different samples of this
1145 sequence (white dot on figure 4). a) Pseudosection computed with Holland and Powell
1146 thermodynamic database (version 1998, updated in 2002) for an average composition of the schists
1147 in the NCKFMASHT system. Outlined on this pseudosection are: stability field of staurolite (light
1148 red area), upper limit of chlorite stability (green line), andalusite (And) to sillimanite (Sil) transition
1149 and muscovite breakdown (black lines), and hydrated granite solidus (red line) b) Compilation of

1150 constrains for all samples in the system NCKFMASHT, the green lines represent the breakdown of
1151 chlorite, the yellow lines are the bounds for the stability field of staurolite, the black lines are the
1152 upper limit for the stability of muscovite, the blue lines represent the upper limit (in terms of
1153 pressure) of stability for cordierite, and red lines are the wet solidus curves; c) Pseudosection
1154 computed with Holland and Powell thermodynamic database (version 1998, updated in 2002) in the
1155 KFMASH system, with TiO₂ projected through ilmenite, CaO projected through anorthite and NaO
1156 projected through albite. d) Pseudosection computed with Domino/Theriak and the SPaC145
1157 thermodynamic database in the KFMASH system (using the same composition than for 6c). See
1158 text for more explanations.

1159

1160

1161 Figure 7: a) BSE image of a garnet from sample 10Ag03 analyzed with EPMA for major elements
1162 determination. The bold black line represents the position of the transect analyzed. b) Garnet end-
1163 members composition along the transect shown on figure 8a. The garnet analyses highlight the
1164 absence of zonation for major elements composition, even near the rim of the grain. Note the
1165 discontinuous scale due to very high almandine content, above 80 % here and commonly above
1166 65% for all garnet compositions.

1167

1168

1169 Figure 8: thermodynamic modelling for the gneissic core, using Holland and Powell
1170 thermodynamic database (version 1998, updated in 2002) and NCKFMASHT system of
1171 components. a) Pseudosection for sample 11AgG03, located near the Castle of Cuxous, close to the
1172 Late Cambrian – Early Ordovician sequence. The shaded area in blue represent the small divariant
1173 field for the dehydration-melting reaction of biotite. Red and green lines are isopleths of garnet
1174 composition, almandine and pyrope contents, respectively. The bold lines for both contents
1175 represent the garnet composition for this sample (see table 2). The brown area between the two bold
1176 lines for isopleths represent the P-T conditions determined for this sample based on the assemblage
1177 and the garnet composition. b) Summary of all kinzigite samples P-T conditions determinations. As
1178 for figure 9a, red lines represent almandine contents of garnets for each sample, and green lines are
1179 pyrope contents, black lines are the upper and lower limits for the biotite dehydration-melting
1180 reaction. c) Cross section with the location and P-T conditions for all kinzigites samples. Those who
1181 are not strictly on the cross section (10Ag03 and 10Ag05) are projected based on their distance to
1182 the boundary between the gneissic core and the late Cambrian – early Ordovician sequence.

1183

1184

1185 Figure 9: Large polarized photomicrographs for the 3 samples used for the geochronological study:
1186 a) 10Ag02; b) 10Ag04; c) 11Ag03. The position of the monazite grains analyzed for U-Th-Pb by
1187 LA ICP-MS are highlighted with yellow circles, with their associated names next to it. The limits of
1188 the field of view (dashed rectangles) used for the figure 6 for the petrological study for samples
1189 10Ag04 (figure 5b) and 11Ag03 (figure 5c) are shown with dashed lines. Normal shear zones are
1190 highlighted for the highly deformed sample 11Ag03 using asymmetric arrows.

1191

1192

1193 Figure 10: Yttrium and Thorium X-ray maps of the different monazite grains analyzed for the U-
1194 Th-Pb geochronology for samples 10Ag02 (A), 10Ag04 (B) and 11Ag03 (C). The white dots on Y
1195 maps represent the location of LA ICP-MS analyses, with the label number. For sample 10Ag04,
1196 monazite grains in inclusion in garnet are labelled with “grt” on top.

1197

1198

1199 Figure 11: Concordia diagrams for all U-Th-Pb analyses of monazite grains. A) Analyses for
1200 sample 10Ag02, close to the Ansignan charnockite, all Y-rich cores define a statistical meaningful
1201 population with an age of 305 ± 4 Ma (2σ). B) Analyses of monazite for the sample 10Ag04, also
1202 close to the charnockite, taking only the spot representing Th/U ratio of 6.5 ± 1 , they define a single
1203 population of ages with a mean of 306 ± 2 Ma (2σ), one very low concordant age has been
1204 excluded. C) Analyses of monazite for sample 11Ag03, the most deformed and retrogressed
1205 kinzigite sample, located in the upper part of the gneissic core. Nine of the analyses successfully
1206 represent a single population of ages, with a mean at 296 ± 2 Ma (2σ). The analyses of m3 have
1207 been excluded as well as the low Th core in m1 (figure 11c). Monazite grain 3 seems to be more
1208 affected by the Cretaceous deformations, with tailing of the ages toward younger values. D)
1209 Analyses of high Th/U zones of monazite grains from sample 10Ag04. 12 of these analyses clearly
1210 define a single population of ages with a mean value of 300 ± 2 Ma (2σ).

1211

1212

1213 Figure 12: Reconstruction of the metamorphic gradient after the main Variscan metamorphic event
1214 with both the gneissic core samples and the late Cambrian – early Ordovician sequence.

1215

1216

1217 Figure 13: reconstruction of the evolution of the geothermal gradient of the Agly massif during the
1218 Late-Variscan HT-LP metamorphic event. a) Intrusion of the magmatic bodies (grey boxes) at
1219 different structural levels of the Agly massif between 308 and 304 Ma, with a lower crustal source

1220 for these magmas, see text. b) At the time of the main metamorphic event (*c.* 305 Ma), geothermal
1221 gradient is directly inferred from the P-T conditions determined from thermodynamic modelling for
1222 the gneissic core (red symbols) c) Reconstruction of the geothermal gradient after the main Late-
1223 Variscan thinning event, at *c.* 296-300 Ma. The late Cambrian – early Ordovician sequence is
1224 slightly heated due to the juxtaposition of the hot gneissic core. Blue areas represent the two main
1225 subtractive zones responsible for the thinning of the massif.

1226 Mineral abbreviations around the alumino-silicate triple point are kyanite (ky), sillimanite (sil),
1227 andalusite (and). The two main dehydration reactions described in the text are highlighted,
1228 muscovite dehydration (ms -) and biotite dehydration melting (bt sil q = grt crd L).

1229

1230

1231 Table 1: XRF analyses of all samples used in this study. GPS location are in the French system
1232 Lambert 2 étendu.

1233

1234 Table 2: Average garnet core analyses from EPMA for kinzigites samples of the gneissic core with
1235 their respective variations, computed as 1 standard deviation (1s). Structural formulae are computed
1236 based on 12 oxygens, the relative proportion of almandine (Alm), pyrope (Py), grossular (Gr) and
1237 spessartine (Sps).

1238

1239 Table 3: Summary of all U-Th-Pb data for monazite used in this study with their respective textural
1240 positions.

1241

1242 Table 4: Summary of P-T conditions for all kinzigite samples, determined from pseudosections (see
1243 figure 8b).

1244

1245

1246